Please cite this article in press as: Maruyama et al., Imaging of Tau Pathology in a Tauopathy Mouse Model and in Alzheimer Patients Compared to Normal Controls, Neuron (2013), http://dx.doi.org/10.1016/j.neuron.2013.07.037



tauopathies. Interestingly, right-side dominant [$^{11}$C]PBB3-PET signals in the basal ganglia were consistent with laterality of atrophy in this area (Figure S8F). These findings may also be associated with a right-side dominant decrease in cerebral blood flow and left-side dominant motor signs in this patient.

## DISCUSSION

Here, we report our efforts to develop BBB-penetrant ligands that are capable of binding to and visualizing intracellular tau aggregates in AD and non-AD tauopathies. These compounds may accordingly be useful for the differential diagnosis of neurological conditions in elderly subjects on the basis of the distribution of tau lesions, thereby opening up novel avenues for research in elucidating mechanisms of tau-mediated neurodegeneration, as well as tau-focused biomarkers and therapies.

Despite numerous efforts to develop imaging ligands to visualize tau pathologies in the brains of patients with AD and related tauopathies, the urgent need for these tau biomarkers remains largely unmet. To address this significant challenge, we also took advantage of a multimodal imaging system, which facilitates a quick and label-free validation of candidate compounds in terms of their transfer to the brain and retention in tau-rich regions. In addition, subcellular-resolution imaging optics exemplified by two-photon laser scanning microscopy provided proof of the rapid transfer of intravenously administered potential tau pathology imaging agents from plasma to the CNS extracellular matrix and subsequently to the cytoplasm of neurons, where they can bind to intracellular tau inclusions. Based on these encouraging preliminary data using nonlabeled compounds, a subset of these compounds was radiolabeled for use in PET imaging of Tg mice that model tau pathology, and a radioligand that yielded the best visualization of tau lesions in these Tg mice was selected for further testing in human AD patients and NC subjects as well as patients with probable CBD. This stepwise strategy enabled us to identify and advance the most promising PET probe for the visualization and quantitative assessment of tau pathology in the CNS of living human subjects. Interestingly, another research group has recently reported development of $^{18}$F-labeled PET ligands for tau lesions mostly through assessments of binding to brain tissues, but not recombinant tau assemblies (Zhang et al., 2012; Chien et al., 2013), as in the present approach. These radioligands have been implied to produce considerably high contrasts for tau pathologies in living AD brains, and relatively long radioactive half-life of $^{18}$F would enable delivery of radioligands from a radiosynthesis sites to multiple PET facilities. [$^{11}$C]PBB3 has distinct advantages over these compounds, as exemplified by affinity for diverse tau lesions, including Tg mouse tau aggregates, applicability to multimodal imaging, and induction of smaller radioactive exposure than $^{18}$F-labeled ligands.

In the present work, we clinically validated the performance of [$^{11}$C]PBB3 as a tau imaging agent by comparing the distribution of [$^{11}$C]PBB3 with that of [$^{11}$C]PIB in AD brains. Tau deposits in patients with moderate or severe AD are thought to be distributed extensively in the neocortical and limbic regions (classified as Braak stage V/VI) (Braak and Braak, 1991), thereby resembling localization of senile plaques, except for the predominance of tau aggregates in the hippocampal formation. This rationalizes the use of radioactivity in the medial temporal area as an index to validate an imaging probe for tau pathology versus Aβ deposits in AD patients from prodromal to advanced stages. Furthermore, our preliminary data suggest that [$^{11}$C]PBB3 may be capable of capturing the temporospatial spreading of neurofibrillary tau pathologies from the limbic system (Braak stage III/IV or earlier) to neocortical areas (Braak stage V/VI) with the progression of AD (Figure 8). A considerable subset of tau lesions at Braak stage I/II is composed of phosphorylated tau deposits barely reactive with thioflavin-S (i.e., pretangles), and NFTs are relatively low in number and are confined to the transentorhinal cortex (Braak and Braak, 1991; Braak et al., 2011). Therefore, detection of these early tau pathologies would be more difficult. Our next-stage clinical study with expanded sample size and wider range of MMSE scores is currently ongoing to pursue tau accumulation in normal controls and subjects with mild cognitive impairments and AD at diverse stages and will bring more compelling insights into the significance of tau PET imaging in early diagnosis and prediction of AD. In addition, alterations of [$^{11}$C]PBB3 retention were indicated in the transition from mild to moderate AD. Loss of PET signals in the lateral temporal cortex of a patient with moderate AD (subject 6 in Figure 8) might not result from atrophy of this region, as the hippocampus of the same subject exhibited strong [$^{11}$C]PBB3 binding despite marked atrophy. Possible explanations for this change include formation of extracellular NFTs and their envelopment by astrocytes in the degenerating neocortex, profoundly modifying accessibility of these NFTs to exogenous molecules (Schmidt et al., 1988). This notion would need to be examined by combined autoradiogarphic and immunohistochemical assays of different brain regions.

Being able to visualize tau deposits with [$^{11}$C]PBB3 in non-AD tauopathies, such as PSP, CBD, and related disorders, is also of major importance, as suggested in the present PET data the support detectability of tau deposition in living CBD brains. As compared with NFTs and neuropil threads in AD, abundant tau deposits are largely confined to specific neuroanatomical locations of the CNS in tau-positive, plaque-negative illnesses, as exemplified by PSP and CBD (Dickson et al., 2011), but the homogenous and low-level background signals of [11C]PBB3 in brain parenchyma indicate the possibility of detecting tau lesions in these disorders. Following such in vivo assessments, a postmortem neuropathological evaluation of scanned subjects would be required as a reference standard for PET assays of non-AD tau pathologies.

[$^{11}$C]PIB-positive plaque formation nearly plateaus prior to the progression of brain atrophy in AD (Engler et al., 2006), but tau abnormalities may bridge the chasm between Aβ fibrillogenesis and neuronal death. Consistent with this notion, our PET/MRI data indicate that the deposition of tau inclusions as visualized by the intense [$^{11}$C]PBB3 labeling but lacking overt [$^{11}$C]PIB binding is closely associated with a local volume reduction in the hippocampal formation. Indeed, our pilot clinical PET study demonstrated that localized accumulation of [$^{11}$C]PBB3 in the medial temporal region of AD patients was accompanied by marked hippocampal atrophy (Figure 7B). Notably, [$^{11}$C]PBB3-PET signals were substantially increased, notwithstanding the atrophy-related partial volume effects on PET images, and this

observation may support the contribution of tau fibrils to toxic neuronal death in AD. However, these data do not immediately imply neurotoxicities of [$^{11}$C]PBB3-reactive tau fibrils, in light of MRI-detectable neurodegeneration uncoupled with [$^{11}$C]PBB3 retention in the hippocampus of PS19 mice. In the hippocampal formation of AD patients, neurons bearing NFTs that resemble those in the PS19 hippocampus may drive neurodegeneration similar to that observed in either the PS19 hippocampus or brain stem, and this issue could be addressed in future studies using [$^{11}$C]PBB3-PET and MRI in diverse mouse models, including PS19 and rTg4510 mice, and human subjects.

Our analyses of multiple β sheet ligands illustrated electrochemical and/or conformational diversities of β-pleated sheets among amyloid aggregates, producing a selectivity of these compounds for a certain spectrum of fibrillar pathologies (Figures 1 and S1). Lipophilicities of the β sheet ligands could determine their reactivity with noncored plaques, as noted among the PBBs studied here (Figure 1), although the molecular properties underlying this variation are yet to be elucidated. Meanwhile, we noted that all β sheet ligands tested in the present study were reactive with dense core plaques regardless of their lipophilicities. This may affect in vivo PET signals, particularly in AD brain areas with abundant cored plaques, such as the precuneus. However, our combined autoradiographic and histochemical assessments indicated that [$^{11}$C]PBB3 bound to dense core plaques accounts for less than 10% of total specific radioligand binding in these areas, and this percentage in fact includes binding to tau fibrils in plaque neurites in addition to Aβ amyloid core. A second possibility to account for the diversity of ligand reactivity to tau lesions may arise from the packing distance between two juxtaposed β sheets in tau filaments and is discussed in the Supplemental Discussion.

Notably, selectivity of [$^{11}$C]PBB3 for tau versus aggregates may depend on free radioligand concentration in the brain. Our autoradiographic binding assays suggested that affinity of [$^{11}$C]PBB3 for NFTs is 40- to 50-fold higher than senile plaques, but binding components on tau fibrils may be more readily saturated by this radioligand than those on Aβ fibrils. [$^{11}$C]PBB3-PET data in humans indicated that uptake of this radioligand into the brain is less than one-third of [$^{11}$C]PIB uptake and that free radioligand concentration in the brain at a pseudoequilibrium state is approximately 0.2 nM or lower. In this range of concentration, [$^{11}$C]PBB3 could preferentially interact with high-affinity binding components formed by tau assemblies. An excessive amount of radioligand in the brain would result in saturation of radioligand binding to tau lesions and increased binding to low-affinity, high-capacity binding components in Aβ plaques, and such overload of free radioligand is more likely in regions with less abundant tau pathologies. This could be even more critical in capturing early tau pathologies that originate in the hippocampal formation and may require technical improvements and methodological refinements, including high-resolution imaging, correction for motions of subjects during scans, and robust definition of VOIs on the atrophic hippocampus.

Although nonspecific [$^{11}$C]PBB3-PET signals in control human subjects were generally low, radioligand retention in dural venous sinuses was noticeable in all scanned individuals. Possible mechanisms that underlie this property are discussed in the Supplemental Discussion.

The present work has also implied the potential utility of multimodal imaging systems for translational development of therapeutic agents that counteract tau fibrillogenesis. Optical imaging with a near-infrared fluorescent probe, such as PBB5, could provide the least invasive technique to assess tau accumulation in living mouse models. As demonstrated by our in vitro and ex vivo fluorescence labeling, all PBBs share a similarity in terms of their reactivity with tau aggregates. Hence, PBB5 optics may be applicable to early screening of therapeutic agents that suppress tau deposition, and the data on abundance of tau lesions obtained by this approach may be translatable to advanced stages of assessments using [$^{11}$C]PBB3-PET in animal models and humans. By contrast, pharmacokinetic properties of PBB5 (Figure S5) were found to be distinct from those of electrically neutral PBBs, including PBB2 and PBB3. These considerations would be of importance in developing and using fluorescent ligands applicable to optical and PET imaging.

To conclude, our class of multimodal imaging agents offers the possibility of visual investigations of fibrillary tau pathologies at subcellular, cellular, and regional levels. These assay systems are potentially powerful tools for the longitudinal evaluation of anti-tau treatments (Marx, 2007), as a single probe may facilitate a seamless, bidirectional translation between preclinical and clinical insights. PET tracers would also serve a more immediate therapeutic purpose by enabling the assessment of the effects of anti-Aβ and anti-tau therapies on tau pathologies in living AD patients.

## EXPERIMENTAL PROCEDURES

### Compounds and Reagents

PBB1 (Wako Pure Chemical Industries), PBB2 (ABX), PBB3 (Nard Institute), PBB4 (ABX), mPBB5 (Nard Institute), desmethyl precursor of [$^{11}$C]PBB2 (2-[4-(4-aminophenyl)buta-1,3-dienyl]benzothiazol-6-ol; Nard Institute), desmethyl precursor of [$^{11}$C]PBB3 protected with a silyl group (5-[4-(6-tert-butyldimethylsilyloxy-benzothiazol-2-yl)buta-1,3-dienyl]pyridine-2-amine; Nard Institute), desmethyl precursor of [$^{11}$C]mPBB5 (2-[4-(4-dimethylaminophenyl) buta-1,3-dienyl]-3-ethyl-6-hydroxybenzothiazol-3-ium; Nard Institute), and 2-[8-(4-dimethylaminophenyl)octa-1,3,5,7-tetraenyl]-3-ethylbenzothiazol-3-ium (DM-POTEB; Nard Institute) were custom synthesized. Information on other chemicals is provided in the Supplemental Experimental Procedures. ClogP for each compound was calculated using ACD Chemsketch logP software (Advanced Chemistry Development).

### Animal Models

Tg mice heterozygous for human T34 (4-repeat tau isoform with 1 N-terminal insert) with FTDP-17 P301S mutation driven by mouse prion protein promoter, also referred to as PS19 mice (Yoshiyama et al., 2007), were bred and kept on a C57BL/6 background. All mice studied here were maintained and handled in accordance with the National Research Council's Guide for the Care and Use of Laboratory Animals and our institutional guidelines. Protocols for the present animal experiments were approved by the Animal Ethics Committees of the National Institute of Radiological Sciences.

### Postmortem Brain Tissues

Procedures for preparation of human and mouse brain sections are given in the Supplemental Experimental Procedures.

### In Vitro and Ex Vivo Fluorescence Microscopy

Six micrometer paraffin sections generated from patient brains and 20 μm frozen sections of mouse brains were stained with $10^{-3}$% β sheet ligands

dissolved in 50% ethanol for 1 hr at room temperature. Images of the fluorescence signals from these compounds were captured by nonlaser (BZ-9000; Keyence Japan) and confocal laser scanning (FV-1000; Olympus) microscopes. In the confocal imaging, excitation/emission wavelengths (nm) were optimized for each compound as follows: 405/420-520 (PBB3, FSB, PIB, BF-227, BF-158, FDDNP, thioflavin-S), 488/520-580 (PBB2, PBB4), 515/530-630 (PBB1, curcumin), and 635/645-720 (PBB5, BF-189, DM-POTEB). Subsequently, the tested samples and adjacent sections probed serially with each ligand were autoclaved for antigen retrieval, immunostained with the anti-tau monoclonal antibody AT8 that is specific for tau phosphorylated at Ser 202 and Thr 205 (Endogen), as well as a polyclonal antibody against AβN3(pE), and inspected using the microscopes noted above. For ex vivo imaging, PS19 and non-Tg WT at 10–12 months of age were anesthetized with 1.5% (v/v) isoflurane and were given 1 mg/kg PBB1-4, 0.1 mg/kg PBB5, or 10 mg/kg FSB by syringe via tail vein. The animals were killed by decapitation at 60 min after tracer administration. Brain and spinal cord were harvested and cut into 10-μm-thick sections on a cryostat (HM560). The sections were imaged using microscopes as in the in vitro assays and were labeled with either FSB or AT8, followed by microscopic re-examination.

### Ex Vivo and In Vivo Multiphoton Imaging

Experimental procedures are given in the Supplemental Experimental Procedures.

### In Vivo and Ex Vivo Pulsed Laser Scanning Imaging

Noninvasive scans of isoflurane-anesthetized non-Tg WT and tau Tg mice at 12 months of age were performed using a small animal-dedicated optical imager (eXplore Optix; ART). Scan protocols are given in the Supplemental Experimental Procedures.

### Radiosynthesis of [$^{11}$C]PBB2

Experimental procedures are given in the Supplemental Experimental Procedures.

### Radiosynthesis of [$^{11}$C]PBB3

[$^{11}$C]Methyl iodide was produced and transferred into 300 μl of dimethyl sulphoxide (DMSO) containing 1.5–2 mg of *tert*-butyldimethylsilyl desmethyl precursor and 10 mg of potassium hydroxide at room temperature. The reaction mixture was heated to 125°C and maintained for 5 min. After cooling the reaction vessel, 5 mg of *tetra-n*-butylammonium fluoride hydrate in 600 μl of water was added to the mixture to delete the protecting group, and then 500 μl of HPLC solvent was added to the reaction vessel. The radioactive mixture was transferred into a reservoir for HPLC purification (CAPCELL PAK $C_{18}$ column, 10 × 250 mm; acetonitrile/50 mM ammonium formate = 4/6, 6 ml/min). The fraction corresponding to [$^{11}$C]PBB3 was collected in a flask containing 100 μl of 25% ascorbic acid solution and 75 μl of Tween 80 in 300 μl of ethanol and was evaporated to dryness under a vacuum. The residue was dissolved in 10 ml of saline (pH 7.4) to obtain [$^{11}$C]PBB3 (970–1,990 GBq at the end of synthesis [EOS]) as an injectable solution. The final formulated product was radiochemically pure (≥95%) as detected by analytic HPLC (CAPCELL PAK $C_{18}$ column, 4.6 × 250 mm; acetonitrile/50 mM ammonium formate = 4/6, 2 ml/min). The specific activity of [$^{11}$C]PBB3 at EOS was 37–121 GBq/μmol, and [$^{11}$C]PBB3 maintained its radioactive purity exceeding 90% over 3 hr after formulation.

### Radiosynthesis of [$^{11}$C]mPBB5

Experimental procedures are given as Supplemental Experimental Procedures.

### Radiosynthesis of [$^{11}$C]PIB

Radiolabeling of PIB was performed as described elsewhere (Maeda et al., 2011). The specific activity of [$^{11}$C]PIB at EOS was 50–110 GBq/μmol.

### In Vitro and Ex Vivo Autoradiography

Experimental procedures are given in the Supplemental Experimental Procedures.

### In Vivo PET Imaging of Mice

PET scans were performed using a microPET Focus 220 animal scanner (Siemens Medical Solutions) immediately after intravenous injection of [$^{11}$C]PBB2 (28.3 ± 10.3 MBq), [$^{11}$C]PBB3 (29.7 ± 9.3 MBq), or [$^{11}$C]mPBB5 (32.8 ± 5.9 MBq). Detailed procedures are provided in the Supplemental Experimental Procedures.

### In Vivo PET Imaging of Humans

Three cognitively normal control subjects (64, 72, and 75 years of age; mean age, 70.3 years) and three AD patients (64, 75 and 77 years of age; mean age, 72 years) were recruited to the present work (Figure 8). Additional information on these subjects is given in the Supplemental Experimental Procedures. The current clinical study was approved by the Ethics and Radiation Safety Committees of the National Institute of Radiological Sciences. Written informed consent was obtained from the subjects or their family members. PET assays were conducted with a Siemens ECAT EXACT HR+ scanner (CTI PET Systems). Detailed PET scan protocols are provided in the Supplemental Experimental Procedures. A fraction of radioactivity corresponding to unmetabolized [$^{11}$C]PBB3 in plasma at 3, 10, 20, 30, and 60 min was determined by HPLC (Waters mBondapak $C_{18}$ column, 7.8 × 300 mm; acetonitrile/ammonium formate mobile phase with gradient elution = 40/60, 52/48, 80/20, 80/20, 40/60, and 40/60 at 0, 6, 7, 8, 9, and 15 min, respectively; flow rate, 6 ml/min) as described elsewhere (Suzuki et al., 1999). The radiotracer injection and following scans and plasma assays were conducted in a dimly lit condition to avoid photoracemization of the chemicals.

Individual MRI data were coregistered to the PET images using PMOD software (PMOD Technologies). Volumes of interest (VOIs) were drawn on coregistered MR images and were transferred to the PET images. Procedures of image analyses are provided in the Supplemental Experimental Procedures.

We additionally carried out PET scans of a patient who was clinically diagnosed as having corticobasal syndrome, as described in the Supplemental Experimental Procedures.

## SUPPLEMENTAL INFORMATION

Supplemental Information includes Supplemental Experimental Procedures, nine figures, and one table and can be found with this article online at http://dx.doi.org/10.1016/j.neuron.2013.07.037.

## ACKNOWLEDGMENTS

The authors thank Mr. T. Minamihisamatsu and Mr. Y. Matsuba for technical assistance, the staff of the Molecular Probe Group, National Institute of Radiological Sciences, for support with radiosynthesis, Dr. Y. Yoshiyama at National Hospital Organization Chiba-East Hospital for his support on clinical PET studies, and Dr. T. Iwatsubo at the University of Tokyo and Dr. H. Inoue at Kyoto University for their critical discussions. This work was supported in part by grants from the National Institute on Aging of the National Institutes of Health (AG10124 and AG17586) (to J.Q.T. and V. M.-Y.L.), Grants-in-Aid for Japan Advanced Molecular Imaging Program, Young Scientists (21791158) (to M.M.), Scientific Research (B) (23390235) (to M.H.), Core Research for Evolutional Science and Technology (to T.S.), Scientific Research on Innovative Areas ("Brain Environment") (23111009) (to M.H.) from the Ministry of Education, Culture, Sports, Science and Technology, Japan, Thomas H. Maren Junior Investigator Fund from College of Medicine, University of Florida (to N.S.), and research fund of Belfer Neurodegeneration Consortium (to Q.C. and M.-K.J.). M.M., H. Shimada, T.S., M.-R.Z., and M.H. are named as inventors on a patent application 0749006WO1, claiming subject matter related to the results described in this paper.

Accepted: July 12, 2013
Published: September 18, 2013

## REFERENCES

Bacskai, B.J., Hickey, G.A., Skoch, J., Kajdasz, S.T., Wang, Y., Huang, G.F., Mathis, C.A., Klunk, W.E., and Hyman, B.T. (2003). Four-dimensional

multiphoton imaging of brain entry, amyloid binding, and clearance of an amyloid-β ligand in transgenic mice. Proc. Natl. Acad. Sci. USA *100*, 12462–12467.

Ballatore, C., Lee, V.M.Y., and Trojanowski, J.Q. (2007). Tau-mediated neurodegeneration in Alzheimer's disease and related disorders. Nat. Rev. Neurosci. *8*, 663–672.

Braak, H., and Braak, E. (1991). Neuropathological stageing of Alzheimer-related changes. Acta Neuropathol. *82*, 239–259.

Braak, H., Thal, D.R., Ghebremedhin, E., and Del Tredici, K. (2011). Stages of the pathologic process in Alzheimer disease: age categories from 1 to 100 years. J. Neuropathol. Exp. Neurol. *70*, 960–969.

Chien, D.T., Bahri, S., Szardenings, A.K., Walsh, J.C., Mu, F., Su, M.Y., Shankle, W.R., Elizarov, A., and Kolb, H.C. (2013). Early clinical PET imaging results with the novel PHF-tau radioligand [F-18]-T807. J. Alzheimers Dis. *34*, 457–468.

Dickson, D.W., Kouri, N., Murray, M.E., and Josephs, K.A. (2011). Neuropathology of frontotemporal lobar degeneration-tau (FTLD-tau). J. Mol. Neurosci. *45*, 384–389.

Engler, H., Forsberg, A., Almkvist, O., Blomquist, G., Larsson, E., Savitcheva, I., Wall, A., Ringheim, A., Långström, B., and Nordberg, A. (2006). Two-year follow-up of amyloid deposition in patients with Alzheimer's disease. Brain *129*, 2856–2866.

Fodero-Tavoletti, M.T., Okamura, N., Furumoto, S., Mulligan, R.S., Connor, A.R., McLean, C.A., Cao, D., Rigopoulos, A., Cartwright, G.A., O'Keefe, G., et al. (2011). $^{18}$F-THK523: a novel *in vivo* tau imaging ligand for Alzheimer's disease. Brain *134*, 1089–1100.

Higuchi, M., Iwata, N., Matsuba, Y., Sato, K., Sasamoto, K., and Saido, T.C. (2005). $^{19}$F and $^{1}$H MRI detection of amyloid β plaques *in vivo*. Nat. Neurosci. *8*, 527–533.

Hintersteiner, M., Enz, A., Frey, P., Jaton, A.L., Kinzy, W., Kneuer, R., Neumann, U., Rudin, M., Staufenbiel, M., Stoeckli, M., et al. (2005). *In vivo* detection of amyloid-β deposits by near-infrared imaging using an oxazine-derivative probe. Nat. Biotechnol. *23*, 577–583.

Klunk, W.E., Wang, Y., Huang, G.F., Debnath, M.L., Holt, D.P., Shao, L., Hamilton, R.L., Ikonomovic, M.D., DeKosky, S.T., and Mathis, C.A. (2003). The binding of 2-(4′-methylaminophenyl)benzothiazole to postmortem brain homogenates is dominated by the amyloid component. J. Neurosci. *23*, 2086–2092.

Klunk, W.E., Engler, H., Nordberg, A., Wang, Y., Blomqvist, G., Holt, D.P., Bergström, M., Savitcheva, I., Huang, G.F., Estrada, S., et al. (2004). Imaging brain amyloid in Alzheimer's disease with Pittsburgh Compound-B. Ann. Neurol. *55*, 306–319.

Krebs, M.R.H., Bromley, E.H., and Donald, A.M. (2005). The binding of thioflavin-T to amyloid fibrils: localisation and implications. J. Struct. Biol. *149*, 30–37.

Kudo, Y., Okamura, N., Furumoto, S., Tashiro, M., Furukawa, K., Maruyama, M., Itoh, M., Iwata, R., Yanai, K., and Arai, H. (2007). 2-(2-[2-Dimethylaminothiazol-5-yl]ethenyl)-6- (2-[fluoro]ethoxy)benzoxazole: a novel PET agent for *in vivo* detection of dense amyloid plaques in Alzheimer's disease patients. J. Nucl. Med. *48*, 553–561.

Maeda, J., Ji, B., Irie, T., Tomiyama, T., Maruyama, M., Okauchi, T., Staufenbiel, M., Iwata, N., Ono, M., Saido, T.C., et al. (2007). Longitudinal, quantitative assessment of amyloid, neuroinflammation, and anti-amyloid treatment in a living mouse model of Alzheimer's disease enabled by positron emission tomography. J. Neurosci. *27*, 10957–10968.

Maeda, J., Zhang, M.R., Okauchi, T., Ji, B., Ono, M., Hattori, S., Kumata, K., Iwata, N., Saido, T.C., Trojanowski, J.Q., et al. (2011). *In vivo* positron emission tomographic imaging of glial responses to amyloid-beta and tau pathologies in mouse models of Alzheimer's disease and related disorders. J. Neurosci. *31*, 4720–4730.

Marx, J. (2007). Alzheimer's disease. A new take on tau. Science *316*, 1416–1417.

Okamura, N., Suemoto, T., Furumoto, S., Suzuki, M., Shimadzu, H., Akatsu, H., Yamamoto, T., Fujiwara, H., Nemoto, M., Maruyama, M., et al. (2005). Quinoline and benzimidazole derivatives: candidate probes for *in vivo* imaging of tau pathology in Alzheimer's disease. J. Neurosci. *25*, 10857–10862.

Santacruz, K., Lewis, J., Spires, T., Paulson, J., Kotilinek, L., Ingelsson, M., Guimaraes, A., DeTure, M., Ramsden, M., McGowan, E., et al. (2005). Tau suppression in a neurodegenerative mouse model improves memory function. Science *309*, 476–481.

Schmidt, M.L., Gur, R.E., Gur, R.C., and Trojanowski, J.Q. (1988). Intraneuronal and extracellular neurofibrillary tangles exhibit mutually exclusive cytoskeletal antigens. Ann. Neurol. *23*, 184–189.

Small, G.W., Kepe, V., Ercoli, L.M., Siddarth, P., Bookheimer, S.Y., Miller, K.J., Lavretsky, H., Burggren, A.C., Cole, G.M., Vinters, H.V., et al. (2006). PET of brain amyloid and tau in mild cognitive impairment. N. Engl. J. Med. *355*, 2652–2663.

Suzuki, K., Takei, M., and Kida, T. (1999). Development of an analyzing system for the sensitive measurement of radioactive metabolites on the PET study. J. Labelled Comp. Radiopharm. *42*, S658–S660.

Thompson, P.W., Ye, L., Morgenstern, J.L., Sue, L., Beach, T.G., Judd, D.J., Shipley, N.J., Libri, V., and Lockhart, A. (2009). Interaction of the amyloid imaging tracer FDDNP with hallmark Alzheimer's disease pathologies. J. Neurochem. *109*, 623–630.

Yang, L., Rieves, D., and Ganley, C. (2012). Brain amyloid imaging—FDA approval of florbetapir F18 injection. N. Engl. J. Med. *367*, 885–887.

Yoshiyama, Y., Higuchi, M., Zhang, B., Huang, S.M., Iwata, N., Saido, T.C., Maeda, J., Suhara, T., Trojanowski, J.Q., and Lee, V.M.Y. (2007). Synapse loss and microglial activation precede tangles in a P301S tauopathy mouse model. Neuron *53*, 337–351.

Zhang, W., Arteaga, J., Cashion, D.K., Chen, G., Gangadharmath, U., Gomez, L.F., Kasi, D., Lam, C., Liang, Q., Liu, C., et al. (2012). A highly selective and specific PET tracer for imaging of tau pathologies. J. Alzheimers Dis. *31*, 601–612.

Zhuang, Z.P., Kung, M.P., Hou, C., Skovronsky, D.M., Gur, T.L., Plössl, K., Trojanowski, J.Q., Lee, V.M.Y., and Kung, H.F. (2001). Radioiodinated styrylbenzenes and thioflavins as probes for amyloid aggregates. J. Med. Chem. *44*, 1905–1914.

JNNP Online First, published on October 16, 2013 as 10.1136/jnnp-2013-306110


RESEARCH PAPER

# Apathy correlates with prefrontal amyloid β deposition in Alzheimer's disease

Takaaki Mori,[1,2] Hitoshi Shimada,[1,3] Hitoshi Shinotoh,[1,4] Shigeki Hirano,[1,5] Yoko Eguchi,[1] Makiko Yamada,[1] Ryuji Fukuhara,[2] Satoshi Tanimukai,[2] Ming-Rong Zhang,[1] Satoshi Kuwabara,[5] Shu-ichi Ueno,[1,2] Tetsuya Suhara[1]

▶ Additional material is published online only. To view please visit the journal online (http://dx.doi.org/10.1136/jnnp-2013-306110).

[1]Molecular Imaging Center, National Institute of Radiological Sciences, Chiba, Japan
[2]Department of Neuropsychiatry, Neuroscience, Ehime University Graduate School of Medicine, Shitsukawa, Toon City, Ehime, Japan
[3]Section for Human Neurophysiology, Research Center for Frontier Medical Engineering, Chiba University, Chiba, Japan
[4]Neurology Chiba, Chiba, Japan
[5]Department of Neurology, Chiba University Graduate School of Medicine, Chiba, Japan

**Correspondence to**
Tetsuya Suhara, Molecular Neuroimaging Program, Molecular Imaging Center, National Institute of Radiological Sciences, 4-9-1 Anagawa, Inage-ku, Chiba-shi, Chiba, 260-8555, Japan; suhara@nirs.go.jp

TM and HS are joint first authors.

**To cite:** Mori T, Shimada H, Shinotoh H, *et al. J Neurol Neurosurg Psychiatry* Published Online First: [*please include* Day Month Year] doi:10.1136/jnnp-2013-306110

## ABSTRACT

**Objective** Neuropsychiatric symptoms affect many patients with Alzheimer's disease (AD). ($^{11}$C)Pittsburgh Compound-B (PIB) positron emission tomography (PET) has enabled the in vivo visualisation of brain amyloid-β (Aβ) deposition. This study exploratively investigated the correlation between brain Aβ deposition measured by ($^{11}$C)PIB PET and neuropsychiatric symptoms in AD.

**Methods** Participants were 28 patients (15 women, 13 men) with PIB-positive AD. Clinical assessments included Mini-Mental State Examination, Clinical Dementia Rating scale, neuropsychiatry inventory (NPI) and frontal assessment battery. All patients underwent three-dimensional T1-weighted MRI and ($^{11}$C)PIB PET. The distribution volume ratio (DVR), an index of ($^{11}$C)PIB retention and, thus, Aβ deposition, was estimated voxel by voxel from ($^{11}$C)PIB PET data with partial volume correction. Voxel-based correlation analysis was performed to assess the relationships between DVR and each NPI subscale. Additionally, voxel-based analysis of covariance (ANCOVA) of the DVR images was performed between Patients with AD with and without each neuropsychiatric symptom. Voxel-based morphometry analysis of MRI was also performed.

**Results** Apathy subscale was correlated with ($^{11}$C)PIB retention in the bilateral frontal and right anterior cingulate. ($^{11}$C)PIB retention was greater in the bilateral frontal cortex of patients with AD with apathy than those of without apathy. Overlapping areas between the two analyses were the bilateral orbitofrontal gyrus and left superior frontal gyrus. Other NPI subscales were not correlated with ($^{11}$C)PIB retention. Voxel-based morphometry analysis of MRI showed no significant cluster of correlation between grey matter volume and NPI subscales.

**Conclusions** This study revealed that prefrontal Aβ deposition correlates with apathy.

## INTRODUCTION

Alzheimer's disease (AD) is the most common form of dementia, accounting for approximately 60% of all dementia cases.[1] AD is characterised by gradual deterioration of cognitive functions including memory, and neuropsychiatric symptoms affect as many as 88% of patients with AD.[2] These neuropsychiatric symptoms, including delusions, hallucinations, agitation, depression, anxiety, euphoria, apathy, disinhibition, irritability and aberrant motor behaviour,[3] have serious adverse consequences for patients and caregivers, such as greater impairment of daily living activities and deteriorating quality of life.[4]

In the last decades, neuroimaging measures, such as MRI, single-photon emission CT (SPECT) and $^{18}$F-flurodeoxyglucose (FDG) positron emission tomography (PET) have revealed some correlations between neuropsychiatric symptoms and specific neural networks.[5] An MRI study revealed negative correlations between delusions and grey matter (GM) volumes in the left frontal lobe, right fronto-parietal cortex and left claustrum, between apathy and GM volumes in the anterior cingulate and bilateral frontal, and agitation and GM volumes in the left insula and bilateral anterior cingulate cortex.[5] Other FDG-PET studies demonstrated a correlation between apathy and the left orbitofrontal region[6] and bilateral anterior cingulate region.[7] Some SPECT studies reported that apathy was positively correlated with perfusion in prefrontal and anterior temporal cortices,[8] or the right amygdala, bilateral temporal, right posterior cingulate, right superior frontal, postcentral and left superior temporal gyrus.[9]

Meanwhile, the development of amyloid imaging radiotracers for PET, represented by ($^{11}$C) Pittsburgh Compound-B (PIB), has enabled the in vivo visualisation of brain amyloid-β (Aβ) deposition,[10] one of the core pathological features of AD. Aβ oligomers are the principal effectors of synaptic dysfunction and loss.[11] Postmortem study of AD has demonstrated strong positive correlation between the load of Aβ oligomers and cognitive decline.[12] Taken together, neuropsychiatric symptoms are correlated with regional brain damage, which could be related to neuronal toxicity of focal Aβ oligomers. Although ($^{11}$C)PIB PET does not detect Aβ oligomers, oligomers aggregate to form ($^{11}$C)PIB-detectable Aβ sheets and Aβ plaques. It has been demonstrated using ($^{11}$C)PIB PET that episodic memory impairment is related to Aβ deposition in the temporal cortex of patients with AD in the predementia stage.[13] However, to the best of our knowledge, there has been no study concerning the correlation between neuropsychiatric symptoms and brain Aβ deposition in patients with AD.

The aim of the present study was to investigate the correlation between brain Aβ deposition and neuropsychiatric symptoms in patients with AD exploratively by using ($^{11}$C)PIB PET with voxel-based whole-brain quantitative analysis.

 

## METHODS

### Subjects

Thirty-one persons clinically diagnosed with AD based on the National Institute of Neurological and Communicative Disease and Stroke/Alzheimer's Disease and Related Disorders Association (NINCDS-ADRDA) criteria were recruited.[14] Three of the patients with AD (9.7%) were diagnosed as PIB-negative by visual assessment of distribution volume ratio (DVR) images of ($^{11}$C)PIB PET (see method for creating DVR images) and were excluded. PIB-negative was defined as lower PIB uptake of any GM region than that of white matter (WM) by visual assessment of the DVR image. The 28 PIB-positive AD subjects were enrolled for further analyses.

Neuropsychiatric symptoms were assessed by neuropsychiatry inventory (NPI),[15] which is composed of 10 subscales: delusions, hallucinations, agitation, depression, anxiety, euphoria, apathy, disinhibition, irritability and aberrant motor behaviour. Subjects were also assessed by Mini-Mental State Examination (MMSE)[16] and Clinical Dementia Rating scale (CDR)[17] to measure the severity of global cognitive impairment, and by frontal assessment battery (FAB)[18] to measure the possible frontal dysfunction related to AD.[19]

The PET study was approved by the institutional review board of the National Institute of Radiological Sciences, Japan. Written informed consent was obtained from all subjects or from their spouses or other close family members.

### Probe synthesis

($^{11}$C)PIB was synthesised according to a previous method, by reaction of 2-(4′-aminophenyl)-6-hydroxy-benzothiazole and ($^{11}$C)methyl triflate.[20] The product had radiochemical purity greater than 96.2%. Specific activity ranged from 35.4 to 221.8 GBq/μ mol at the time of injection.

### PET scan

PET images were acquired by Siemens ECAT EXACT HR+ scanner (CTI PET Systems, Knoxville, Tennessee, USA) with an axial field of view of 155 mm, providing 63 contiguous 2.46 mm slices, with 5.6 mm transaxial and 5.4 mm axial resolution. A 10 min transmission scan was performed to measure tissue attenuation. Dynamic emission scan data were acquired in three-dimensional mode for a period of 90 min. Subjects were examined with their eyes closed and their ears unplugged in a quiet room, and their heads were restrained with a band extending across the forehead attached to the headrest. An examiner carefully monitored head movement with laser beams during each scan, and corrections were made when necessary. A dose (370 ±34 MBq in 5 mL) of ($^{11}$C)PIB was intravenously injected for 60 s by infusion pump into the right cubital vein. The PET measurement protocol was based on a previously reported method,[20 21] with some modifications. Briefly, a sequence of 19 scans was acquired during 90 min (3×20 s, 3×40 s, 1×1 min, 2×3 min, 5×6 min, 5×10 min) after ($^{11}$C)PIB injection. All data processing and image reconstruction were performed using standard Siemens software including scatter correction.

### MRI acquisition

MR images were obtained on 1.5 T Intera (Phillips Medical Systems, Best, The Netherlands) on the same day as the PET study. Subjects were scanned with a 3D T1-weighted turbo gradient echo sequence (repetition time (TR) range/echo time (TE) range, 16 msec/5.2 ms; field of view, 256 mm; matrix, 256×256; 196 contiguous axial slices of 1.0 mm thickness).

### PET data analysis

Correction of ($^{11}$C)PIB PET data for partial volume effects was performed with an algorithm implemented in the PMOD software package (PMOD V.3.2; Technologies, Adliswil, Switzerland). This correction is based on the assumption that WM uptake is homogeneous. All brain pixels are classified as WM or GM and sorted into respective segments. Based on these segments and the assumed PET resolution, the spill-out from WM to GM can be estimated and subtracted. Similarly, the spill-out from GM to the surroundings can be estimated and compensated for. The result is a GM image with corrected activity values in all pixels. This method was introduced by Müller–Gärtner *et al.*[22] The parameters were performed as Point Spread Function FWHM: 2.0×2.0×2.0 mm, Correction mode: GM spill-out and spill-in. WM estimation: regression 0.95, and GM threshold: 0.3. All imaging data were then preprocessed and analysed with statistical parametric mapping software (SPM5, Wellcome Department of Cognitive Neurology, London, UK), operating in the Matlab software environment (V.7.10; MathWorks, Natick, Massachusetts, USA). Each T1-weighted MRI scan was coregistered to each PET image, and the spatial normalisation of the MRI images to the SPM5 T1 MRI template was applied to PET images.

A voxel-based DVR was estimated using Logan plot graphical analysis with the cerebellum as reference region by custom software designed by IDL (V.6.0; Jicoux Datasystems, Tokyo, Japan) from ($^{11}$C)PIB PET data.

First, a voxel-based correlation analysis was performed to assess the relationships between DVR and each NPI subscale using SPM5. Age, gender, education years, MMSE and FAB scores were also included in the model as covariates for all symptoms. Second, we performed voxel-based analysis of covariance (ANCOVA) of the DVR images between patients with AD with and without each neuropsychiatric symptom, adjusting for differences in age, gender, years of education, MMSE and FAB scores. FAB score was used as a covariate to remove the effects of frontal dysfunction, such as executive function and specific brain regions which are solely related to NPI symptoms.[19 23] Patients with AD with neuropsychiatric symptoms were defined with a cut-off score of 1 for each NPI subscale.

### Voxel-based morphometry

We performed voxel-based morphometry to clarify the effect of GM atrophy, as a past study reported that GM atrophy was associated with some neuropsychiatric symptoms.[6] T1-weighted images were segmented into GM, WM and cerebrospinal fluid. In SPM5, spatial normalisation, segmentation and modulation are processed by means of a unified segmentation algorithm using SPM5.[24 25] The segmented and modulated normalised GM images were smoothed with a 12 mm FWHM Gaussian kernel. Total intracranial volume (TIV) was computed using the native-space tissue maps of each subject. TIV was included in the model as covariate in the voxel-based morphometry (VBM) analyses. The correlations between GM volumes and each NPI subscale were also analysed. Additionally, ANCOVA of GM volumes between patients with AD with and without neuropsychiatric symptoms was performed. In these analyses, besides TIV, age, gender and education years, also included in the model as covariates were the MMSE and FAB scores.

### Statistical analysis

Group comparisons in demographic variables were performed by Fisher's exact test for gender ratio and CDR, and Student t test for

the others. Statistical analyses were performed using Statistical Package for the Social Sciences software (SPSS V.19, SPSS, Chicago, Illinois, USA). In SPM voxel-based correlation analyses and ANCOVA analyses, false discovery rate (FDR) corrected, $p<0.05$ was considered significant. The extent thresholds were defined as >500 in correlation analyses, and >200 in ANCOVA.

## RESULTS

Twenty-eight patients with AD (15 women, 13 men), aged from 56 to 85 years, were the participants in this study. Their demographic and clinical data are presented in table 1, and their neuropsychiatric symptoms are shown in table 2. Apathy was the most frequent neuropsychiatric symptom (39.2%), while hallucinations and euphoria were rare (7.1%).

Voxel-based correlation analysis of ($^{11}$C)PIB DVR images showed that apathy subscale was significantly correlated with ($^{11}$C)PIB retention in the bilateral middle frontal gyrus, bilateral orbitofrontal gyrus, bilateral medial frontal gyrus, bilateral inferior frontal gyrus, bilateral superior fontal gyrus, bilateral insula, and right anterior cingulate gyrus (FDR, corrected $p<0.05$, cluster extent >500 voxels, voxel size: 2×2×2 mm) (table 3, figure 1). Additionally, the correlation between NPI apathy scale and prefrontal. ($^{11}$C)PIB DVR was confirmed in the volume of interest analysis without partial volume correction ($r^2=0.374$, $p<0.05$, see online supplementary figure E-1). SPM analysis did not show any significant cluster of correlation between any other neuropsychiatric symptom subscale and ($^{11}$C)PIB retention except apathy.

Voxel-based ANCOVA of the DVR images between patients with AD with and without each of the neuropsychiatric symptoms showed greater ($^{11}$C)PIB retention in 11 patients with AD with apathy in the bilateral superior frontal gyri, bilateral orbitofrontal gyri, bilateral medial frontal gyri, right middle frontal gyrus, and right middle temporal gyrus than in the 17 without apathy (FDR, corrected $p<0.05$, cluster extent >200 voxels, voxel size: 2×2×2 mm) (figure 2). There were no significant differences in gender, MMSE, education, FAB, NPI, disease duration and CDR (all $p>0.05$), and only age of the patients with AD with apathy was significantly lower compared with those without ($p<0.01$) (table 4). Voxel-based ANCOVA did not show any significant ($^{11}$C)PIB retention cluster in other neuropsychiatric symptoms except apathy. The overlapping areas between correlation and two-sample analyses were the bilateral orbitofrontal gyri and left superior frontal gyrus (figure 3).

SPM analysis of T1-weighted MRI did not show any significant cluster of correlation between GM volume and any NPI subscale score. Voxel-by-voxel ANCOVA of GM volume between patients with AD with and without neuropsychiatric symptoms did not show any significant cluster in any neuropsychiatric subscale.

Table 1 Demographics and clinical scores

| | Mean (SD) |
|---|---|
| Age (years) | 73.9 (7.9) |
| Gender (F/ M) | 15/13 |
| MMSE | 19.9 (5.1) |
| Education (years) | 11.1 (3.5) |
| CDR score (0:0.5:1:2:3) | 0:15:9:3:1 |
| FAB | 12.1 (3.3) |
| NPI | 4.6 (5.0) |
| Disease duration (years) | 2.8 (1.6) |

CDR, Clinical Dementia Rating scale; FAB, frontal assessment battery; MMSE, Mini-Mental State Examination; NPI, neuropsychiatry inventory.

Table 2 Prevalence and scores of NPI subscales

| | Symptom-presenting subjects | NPI score of all subjects | NPI score of symptom-presenting subjects | |
|---|---|---|---|---|
| | n (%) | Mean (SD) | Mean (SD) | Range |
| Delusions | 4 (14.2) | 0.25 (0.79) | 1.75 (1.50) | 1–4 |
| Hallucinations | 2 (7.1) | 0.10 (0.41) | 1.50 (0.70) | 1–2 |
| Agitation | 6 (21.4) | 0.60 (1.66) | 2.83 (2.71) | 1–8 |
| Depression | 7 (25.0) | 0.71 (1.73) | 2.85 (2.54) | 1–3 |
| Anxiety | 6 (21.4) | 0.25 (0.51) | 1.16 (0.40) | 1–2 |
| Euphoria | 2 (7.1) | 0.07 (0.26) | 1.00 (0.00) | 1–1 |
| Apathy | 11 (39.2) | 1.28 (2.03) | 3.27 (2.00) | 1–8 |
| Disinhibition | 4 (14.2) | 0.17 (0.47) | 1.25 (0.50) | 1–2 |
| Irritability | 9 (32.1) | 0.85 (1.77) | 2.66 (2.31) | 1–8 |
| Aberrant motor behaviour | 4 (14.2) | 0.35 (1.06) | 2.50 (1.73) | 1–4 |
| NPI total | 24 (85.7) | 4.67 (5.02) | 5.45 (5.02) | 1–25 |

Number (%) and scores of NPI subscales of Alzheimer's disease patients. Apathy was the most frequent neuropsychiatric symptom (39.2%), while hallucinations and euphoria were rare (7.1%).
NPI, neuropsychiatry inventory.

## DISCUSSION

We performed an exploratory study of the correlation between ($^{11}$C)PIB retention and neuropsychiatric symptoms. We introduced a cross-validation approach to detect any robust relationship between them. A positive correlation was found between apathy severity and ($^{11}$C)PIB retention in the bilateral superior, middle and inferior frontal gyri; bilateral orbitofrontal gyri, bilateral medial frontal gyri, bilateral insula and right anterior cingulate gyrus. Moreover, patients with AD with apathy showed increased ($^{11}$C)PIB retention in the bilateral superior frontal gyri, bilateral orbitofrontal gyri, bilateral medial frontal gyri, right middle frontal gyrus, and right middle temporal gyrus, when compared with those without apathy. Overlapping areas were the bilateral orbitofrontal gyri and left superior frontal gyrus. We did not find any significant correlation between GM volume and neuropsychiatric symptoms. This is the first study to reveal the correlation between brain Aβ deposition and neuropsychiatric symptoms in patients with AD by the use of ($^{11}$C)PIB PET with voxel-based whole-brain quantitative analysis.

Several neuroimaging studies have reported the specific brain region responsible for apathy in patients with AD. Previous FDG PET studies reported reduced glucose metabolism in the bilateral anterior cingulate region extending inferiorly to the medial orbitofrontal region and bilateral medial thalamus,[7] or hypometabolism in left orbitofrontal regions[6] in patients with AD with apathy compared with those without. SPECT studies reported that patients with AD with apathy were associated with hypoperfusion in prefrontal and anterior temporal cortices,[8] or the right amygdala, bilateral temporal, right posterior cingulate, right superior frontal, postcentral and left superior temporal gyri.[9] An MRI study reported greater cortical thinning in the left caudal anterior cingulate cortex and left lateral orbitofrontal cortex, and left superior and ventrolateral frontal regions in patients with AD with apathy than in those without.[26] Another MRI study revealed that apathy was

Table 3 Location, Z score and cluster size of significantly positive correlation between apathy and ($^{11}$C) Pittsburgh Compound-B (PIB) retention

| | | Peak coordinates (MNI) | | | | |
|---|---|---|---|---|---|---|
| | Brodmann area | X | y | z | Z score | Cluster size |
| Right middle frontal gyrus* | 8 | 26 | 20 | 42 | 5.33 | 1960 |
| Right anterior cingulate gyrus | 32 | 18 | 12 | 44 | 4.66 | 1960 |
| Right medial frontal gyrus | 8 | 14 | 32 | 40 | 4.24 | 1960 |
| Right superior frontal gyrus | 10 | 20 | 60 | 8 | 3.21 | 1960 |
| Left orbitofrontal gyrus | 11 | −4 | 40 | −26 | 3.03 | 1960 |
| Right orbitofrontal gyrus | 11 | 16 | 54 | −16 | 2.99 | 1960 |
| Right inferior frontal gyrus | 44 | 50 | 8 | 24 | 4.61 | 1544 |
| Right insula | 13 | 50 | −22 | 26 | 4.36 | 1544 |
| Left medial frontal gyrus | 8 | −12 | 24 | 44 | 4.17 | 990 |
| Left middle frontal gyrus | 8 | −24 | 26 | 44 | 3.87 | 990 |
| Left superior frontal gyrus | 6 | −12 | 6 | 60 | 3.70 | 990 |
| Left insula | 13 | −36 | 16 | 10 | 3.93 | 604 |
| Left inferior frontal gyrus | 47 | −36 | 32 | 4 | 3.70 | 604 |

Voxel-based positron emission tomography image correlation analysis showed that apathy subscale was significantly correlated with ($^{11}$C)PIB retention (FDR-corrected p<0.05, extent threshold >500 voxels).
*Family-wise error (FWE)–corrected, p<0.05, extent threshold >200 voxels.
FDR, false discovery rate; MNI, Montreal Neurological Institute.

associated with GM density loss in the bilateral anterior cingulate and bilateral frontal cortex, head of the left caudate nucleus and the bilateral putamen in patients with AD.[5] There is evidence that regional patterns of amyloid deposition may not match the patterns of glucose metabolism or GM loss in the brain of AD.[27 28] However, we found a relationship between apathy and ($^{11}$C)PIB retention in the bilateral orbitofrontal gyri and right superior frontal gyrus of patients with AD, which was in agreement with these prior neuroimaging findings in terms of brain regions.[5–9]

A neuropathological study demonstrated that chronic apathy and total NPI composite scores were correlated with anterior cingulate neurofibrillary tangles, but not neuritic plaques in AD brains,[29] a result discordant with our findings. This discrepancy could be explained by the fact that AD brains were obtained at an advanced disease stage in the neuropathological study, while

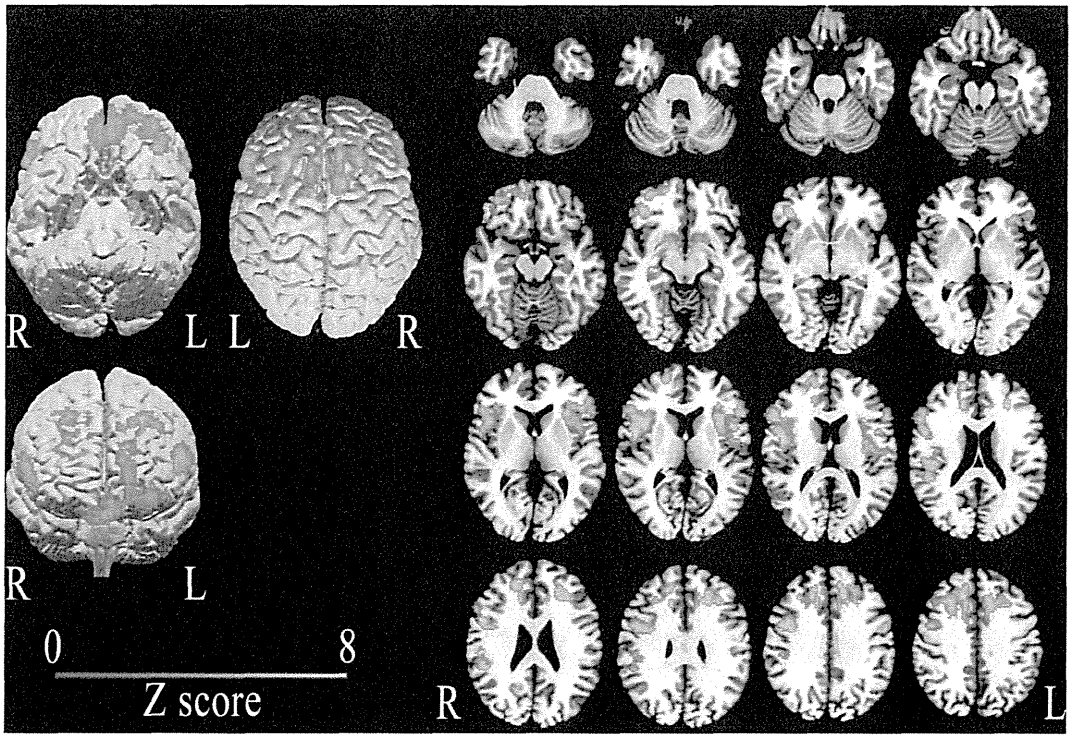


Figure 1 Images of voxel-based maps of significant correlation between neuropsychiatry inventory apathy score and ($^{11}$C) Pittsburgh Compound-B (PIB) retention (false discovery rate, corrected p<0.05, extent threshold >500 voxels). On the left are render images, and on the right axial images. Apathy score was significantly correlated with ($^{11}$C)PIB retention in bilateral middle frontal gyri, bilateral orbitofrontal gyri, bilateral medial frontal gyri, bilateral inferior frontal gyri, bilateral superior fontal gyri, bilateral insula and right anterior cingulate gyrus.

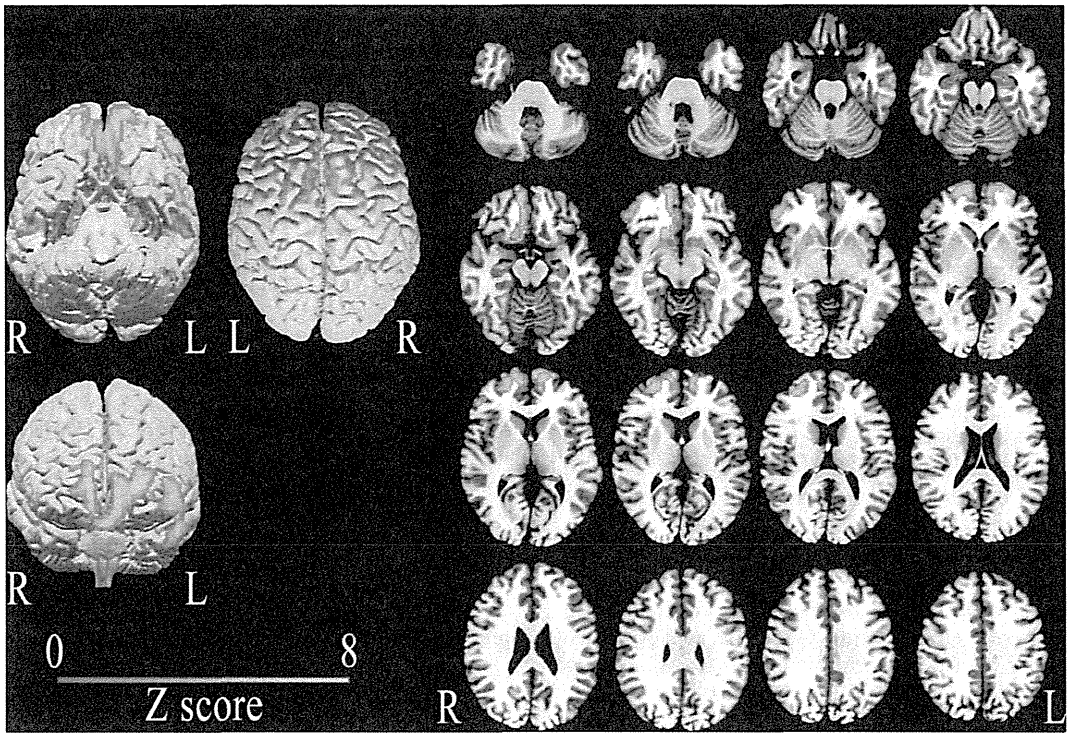


Figure 2 Images voxel-based maps with more ($^{11}$C) Pittsburgh Compound-B (PIB) retention in the Alzheimer's disease (AD) group with apathy than in the AD group without apathy by ANCOVA (false discovery rate, corrected p<0.05, extent threshold >200 voxels). On the left are render images, and on the right axial images. ($^{11}$C)PIB retention of patients with AD with apathy was greater in the bilateral superior frontal gyri, bilateral orbitofrontal gyri, bilateral medial frontal gyri, right middle frontal gyrus and right middle temporal gyrus than in those without apathy.

we measured Aβ deposition in patients with AD in the early disease stage in vivo.

In vitro and in vivo studies have shown that Aβ oligomers reduce glutamatergic synaptic transmission strength and plasticity,[30] and in mice transgenic for human amyloid precursor protein, pathologically elevated levels of Aβ promote the formation of pathogenic Aβ oligomers and cause wide fluctuations in the neuronal expression of synaptic activity-regulated genes,[31] epileptiform activity and non-convulsive seizures.[31] Aβ deposition also increases the proportion of abnormally hyperactive neurons in cortical circuits.[32] ($^{11}$C)PIB has been demonstrated to bind to fibrillar Aβ in diffuse, cored and neuritic plaques, but not to Aβ oligomers,[33] whereas, Aβ oligomers aggregate to form Aβ sheets and Aβ plaques. Therefore, brain regions with high ($^{11}$C)PIB retention could have greater amounts of Aβ oligomers than brain regions with modest ($^{11}$C)PIB retention at least in the early or preclinical stage of AD. It has been demonstrated that healthy elderly individuals with high ($^{11}$C)PIB retention show accelerated cortical atrophy, suggesting that the Aβ load is toxic to local brain regions at the preclinical stage of AD. Taken together, prominent Aβ deposition in the orbitofrontal and superior frontal gyri is thought to play a role in the neuropsychiatric symptom of apathy in patients with AD in the present study.

Table 4 Demographics and clinical scores of apathy-present group and apathy-free group

| | AD group with apathy (n=11) Mean (SD) | AD group without apathy (n=17) Mean (SD) | p Value |
|---|---|---|---|
| Age | 68.5 (7.9) | 77.4 (5.9) | <0.01 |
| Gender (M/F) | 5/6 | 8/9 | 1.00 |
| MMSE | 18.0 (4.7) | 21.1 (5.1) | 0.12 |
| Education | 10.9 (3.6) | 11.2 (3.5) | 0.78 |
| CDR score (0:0.5:1:2:3) | 0:4:5:1:1 | 0:11:4:2:0 | 0.25 |
| FAB | 11.0 (3.3) | 12.7 (3.2) | 0.20 |
| NPI total score | 5.9 (3.4) | 3.8 (5.7) | 0.30 |

Age, MMSE, education, FAB, NPI total score were examined using Student t test. Gender and CDR sore were examined using Fisher's exact test.
AD, Alzheimer's disease; CDR, Clinical Dementia Rating scale; FAB, frontal assessment battery; MMSE, Mini-Mental State Examination; NPI, neuropsychiatry inventory.

In this study, we demonstrated that Aβ deposition in the orbitofrontal and superior frontal gyri is related to apathy in patients with AD, while GM volume in those areas was not correlated with apathy in patients with AD, or differed between patients with AD with and without apathy. The current hypothetical model suggests that Aβ peptide accumulation is a key early event in the pathophysiological process of AD, followed by synaptic dysfunction identified by FDG PET, and subsequent neural loss demonstrated by structural MRI progresses.[34 35] Increased ($^{11}$C)PIB retention in the frontal cortex may be an early marker of cortical damage in AD, and apparent atrophy may follow as the disease progresses. Another possible cause for the absent correlation between GM volume and apathy in this study may be that the AD group without apathy was older than the AD group with apathy.

It has been established that damage of the anterior cingulate circuit presents with apathy,[36] and that the neurons project to the ventral striatum that includes the olfactory tubercle.[36] The function of the anterior cingulate cortex relates to the initiation


**Figure 3** Overlapped ($^{11}$C) Pittsburgh Compound-B retention area between correlation and ANCOVA analyses in apathy. The bilateral orbitofrontal gyrus and left superior frontal gyrus are correlated with apathy in Alzheimer's disease.

and motivational drivers for goal-directed activities, and therefore, damage to this cortical structure would likely lead to a degree of behavioural and cognitive inertia.[37 38] The orbitofrontal afferents provide information regarding the emotional relevance of external stimuli to the anterior cingulate circuit from internal and external environments,[36] and the medial orbitofrontal region has mutual connections with the anterior cingulate and medial dorsal nucleus of the thalamus.[39] Cholinergic neurons originate from the basal nucleus of Meynert and project to frontal limbic cortical regions.[39] Cholinergic dysfunction may also contribute to apathy, because some studies have demonstrated that cholinesterase inhibitors improved apathy in patients with AD.[40]

A previous study using MRI demonstrated that delusions were associated with decreased GM density in the left frontal lobe, right frontoparietal cortex and left claustrum, and agitation was associated with decreased GM volumes in the left insula and bilateral anterior cingulate cortex.[5] Another study using FDG-PET reported that depression was associated with hypometabolism in bilateral dorsolateral prefrontal regions.[6] We did not find any correlation between ($^{11}$C)PIB retention and other neuropsychiatric symptoms except apathy, which probably resulted from the lack of, or only mild symptoms of, delusion, agitation and depression in the patients with AD in the present study.

The limitations of this exploratory study are its small sample size, and mild NPI symptoms including apathy. Although apathy was the most prevalent symptom, less than half the subjects exhibited apathy in this study. PIB retention is well known to have a predilection for the frontal lobes. Taken together, a correlation observed with overall mild NPI apathy symptoms might suggest that frontal PIB retention is a sensitive marker of apathy symptoms, but not necessarily a very specific one. Further studies in a larger number of patients with AD with NPI symptoms will be needed to confirm the correlation between prefrontal ($^{11}$C)PIB retention and the severity of apathy, and reveal a correlation with ($^{11}$C)PIB retention and other neuropsychiatric symptoms besides apathy, which may help to clarify the involved mechanisms and brain circuits, and lead to new insights into the pathophysiology of patients with AD.

**Contributors** Study concept/design: TM, HShim, HShin, SHira. Data analysis/interpretation: TM, HShim, HShin, SHira, YE. Manuscript preparation: TM, HShim, HShin, SHira, YE, MY, RF, ST, M-RZ, SK, S-cU, TS.

**Funding** Dr Kuwabara is funded by Grants-in-Aid for Scientific Research from the Ministry of Education, Culture, Sports, Science and Technology of Japan (23591267, 20590988, 20591018, 23591269), and a Grant-in-Aid for Scientific Research from the Ministry of Health, Labour and Welfare of Japan (JMA-IIA00046), and serves as Associate Editor of *'Journal of Neurology, Neurosurgery, and Psychiatry'*, Editor of *'Internal Medicine'*, and Editorial Board member of *'Clinical Neurophysiology'*. Dr Ueno is funded by a Health and Labour Science Research Grant from the Japanese Ministry of Health, Labour and Welfare, and a Grant-in-Aid for Scientific Research from the Japanese Ministry of Education, Culture, Sports, Science and Technology (23659567). Dr Suhara is funded by the Ministry of Education, Culture, Sports, Science and Technology of Japan, the Strategic Research Program for Brain Sciences and Molecular Imaging Program, and serves as an Editorial Board member of *'International Journal of Neuropsychopharmacology'*, *'Psychogeriatrics'* and *'Current Psychiatry Review'*.

**Competing interests** A part of this study is the result of 'Integrated research on neuropsychiatric disorders' carried out under the Strategic Research Program for Brain Sciences by the Ministry of Education, Culture, Sports, Science and Technology of Japan, 'Japan Advanced Molecular Imaging Program (J-AMP)' of the Ministry of Education, Culture, Sports, Science and Technology (MEXT), Japan, a Grant-in-Aid for Scientific Research on Innovative Areas from the Ministry of Education, Culture, Sports, Science and Technology, Japan, and a Grant-in-Aid for Comprehensive Research on Dementia (No. 11103404) from the Ministry of Health, Labour and Welfare, Japan.

**Patient consent** Obtained.

**Ethics approval** The Institutional Review Board of the National Institute of Radiological Sciences.

**Provenance and peer review** Not commissioned; externally peer reviewed.

## REFERENCES

1 Small GW, Rabins PV, Barry PP, *et al*. Diagnosis and treatment of Alzheimer disease and related disorders. Consensus statement of the American Association for Geriatric Psychiatry, the Alzheimer's Association, and the American Geriatrics Society. *JAMA* 1997;278:1363–71.
2 Mega MS, Cummings JL, Fiorello T, *et al*. The spectrum of behavioral changes in Alzheimer's disease. *Neurology* 1996;46:130–5.
3 Frisoni GB, Rozzini L, Gozzetti A, *et al*. Behavioral syndromes in Alzheimer's disease: description and correlates. *Dement Geriatr Cogn Disord* 1999;10:130–8.
4 González-Salvador T, Lyketsos CG, Baker A, *et al*. Quality of life in dementia patients in long-term care. *Int J Geriatr Psychiatry* 2000;15:181–9.
5 Bruen PD, McGeown WJ, Shanks MF, *et al*. Neuroanatomical correlates of neuropsychiatric symptoms in Alzheimer's disease. *Brain* 2008;131:2455–63.
6 Holthoff VA, Beuthien-Baumann B, Kalbe E, *et al*. Regional cerebral metabolism in early Alzheimer's disease with clinically significant apathy or depression. *Biol Psychiatry* 2005;57:412–21.
7 Marshall GA, Monserratt L, Harwood D, *et al*. Positron emission tomography metabolic correlates of apathy in Alzheimer disease. *Arch Neurol* 2007;64:1015–20.
8 Craig AH, Cummings JL, Fairbanks L, *et al*. Cerebral blood flow correlates of apathy in Alzheimer disease. *Arch Neurol* 1996;53:1116–20.
9 Kang JY, Lee JS, Kang H, *et al*. Regional cerebral blood flow abnormalities associated with apathy and depression in Alzheimer disease. *Alzheimer Dis Assoc Disord* 2012;26:217–24.
10 Klunk WE, Engler H, Nordberg A, *et al*. Imaging brain amyloid in Alzheimer's disease with Pittsburgh Compound-B. *Ann Neurol* 2004;55:306–19.
11 Walsh DM, Klyubin I, Fadeeva JV, *et al*. Naturally secreted oligomers of amyloid beta protein potently inhibit hippocampal long-term potentiation in vivo. *Nature* 2002;416:535–9.
12 Näslund J, Haroutunian V, Mohs R, *et al*. Correlation between elevated levels of amyloid beta-peptide in the brain and cognitive decline. *JAMA* 2000;283:1571–7.
13 Chételat G, Villemagne VL, Pike KE, *et al*. Independent contribution of temporal beta-amyloid deposition to memory decline in the pre-dementia phase of Alzheimer's disease. *Brain* 2011;134:798–807.
14 McKhann G, Drachman D, Folstein M, *et al*. Clinical diagnosis of Alzheimer's disease: report of the NINCDS-ADRDA Work Group under the auspices of Department of Health and Human Services Task Force on Alzheimer's Disease. *Neurology* 1984;34:939–44.
15 Cummings JL, Mega M, Gray K, *et al*. The Neuropsychiatric Inventory: comprehensive assessment of psychopathology in dementia. *Neurology* 1994;44:2308–14.
16 Folstein MF, Folstein SE, McHugh PR. Mini-mental state. A practical method for grading the cognitive state of patients for the clinician. *J Psychiatr Res* 1975;12:189–98.
17 Morris JC. The Clinical Dementia Rating (CDR): current version and scoring rules. *Neurology* 1993;43:2412–4.
18 Dubois B, Slachevsky A, Litvan I, *et al*. The FAB: a frontal assessment battery at bedside. *Neurology* 2000;55:1621–26.
19 Starr JM, Lonie J. Relationship between behavioural and psychological symptoms of dementia and cognition in Alzheimer's disease. *Dement Geriatr Cogn Disord* 2007;24:343–7.

20 Price JC, Klunk WE, Lopresti BJ, *et al*. Kinetic modeling of amyloid binding in humans using PET imaging and Pittsburgh Compound-B. *J Cereb Blood Flow Metab* 2005;25:1528–47.
21 Lopresti BJ, Klunk WE, Mathis CA, *et al*. Simplified quantification of Pittsburgh Compound B amyloid imaging PET studies: a comparative analysis. *J Nucl Med* 2005;46:1959–72.
22 Müller-Gärtner HW, Links JM, Prince JL, *et al*. Measurement of radiotracer concentration in brain gray matter using positron emission tomography: MRI-based correction for partial volume effects. *J Cereb Blood Flow Metab* 1992; 12:571–83.
23 Yamao A, Nagata T, Shinagawa S, *et al*. Differentiation between amnestic-mild cognitive impairment and early-stage Alzheimer's disease using the Frontal Assessment Battery test. *Psychogeriatrics* 2011;11:235–41.
24 Ashburner J, Friston KJ. Unified segmentation. *Neuroimage* 2005;26:839–51.
25 Ashburner J, Friston KJ. Voxel-based morphometry–the methods. *Neuroimage* 2000;1:805–21.
26 Tunnard C, Whitehead D, Hurt C, *et al*. Apathy and cortical atrophy in Alzheimer's disease. *Int J Geriatr Psychiatry* 2011;26:741–8.
27 Edison P, Archer HA, Hinz R, *et al*. Amyloid, hypometabolism, and cognition in Alzheimer disease: an [11C]PIB and [18F]FDG PET study. *Neurology* 2007;68:501–8.
28 Frisoni GB, Lorenzi M, Caroli A, *et al*. In vivo mapping of amyloid toxicity in Alzheimer disease. *Neurology* 2009;72:1504–11.
29 Marshall GA, Fairbanks LA, Tekin S, *et al*. Neuropathologic correlates of apathy in Alzheimer's disease. *Dement Geriatr Cogn Disord* 2006;21:144–7.
30 Chapman PF, White GL, Jones MW, *et al*. Impaired synaptic plasticity and learning in aged amyloid precursor protein transgenic mice. *Nat Neurosci* 1999;2:271–6.
31 Palop JJ, Chin J, Roberson ED, *et al*. Aberrant excitatory neuronal activity and compensatory remodeling of inhibitory hippocampal circuits in mouse models of Alzheimer's disease. *Neuron* 2007;55:697–711.
32 Busche MA, Eichhoff G, Adelsberger H, *et al*. Clusters of hyperactive neurons near amyloid plaques in a mouse model of Alzheimer's disease. *Science* 2008;321:1686–9.
33 Beckett TL, Webb RL, Niedowicz DM, *et al*. Postmortem Pittsburgh Compound B (PiB) binding increases with Alzheimer's disease progression. *J Alzheimers Dis* 2012;32:127–38.
34 Jack CR Jr, Knopman DS, Jagust WJ, *et al*. Hypothetical model of dynamic biomarkers of the Alzheimer's pathological cascade. *Lancet Neurol* 2010; 9:119–28.
35 Sperling RA, Aisen PS, Beckett LA, *et al*. Toward defining the preclinical stages of Alzheimer's disease: recommendations from the National Institute on Aging-Alzheimer's Association workgroups on diagnostic guidelines for Alzheimer's disease. *Alzheimers Dement* 2011;7:280–92.
36 Tekin S, Cummings JL. Frontal-subcortical neuronal circuits and clinical neuropsychiatry: an update. *J Psychosom Res* 2002;53:647–54.
37 Allman JM, Hakeem A, Erwin JM, *et al*. The anterior cingulate cortex. The evolution of an interface between emotion and cognition. *Ann N Y Acad Sci* 2001;935:107–17.
38 Devinsky O, Morrell MJ, Vogt BA. Contributions of anterior cingulate cortex to behavior. *Brain* 1995;118:279–306.
39 Mega MS, Cummings JL, Salloway S, *et al*. The limbic system: an anatomic, phylogenetic, and clinical perspective. *J Neuropsychiatry Clin Neurosci* 1997;9:315–30.
40 Waldemar G, Gauthier S, Jones R, *et al*. Effect of donepezil on emergence of apathy in mild to moderate Alzheimer's disease. *Int J Geriatr Psychiatry* 2011;26:150–7.

Shidahara *et al. EJNMMI Research* 2013, **3**:32
http://www.ejnmmires.com/content/3/1/32

EJNMMI Research
a SpringerOpen Journal

ORIGINAL RESEARCH Open Access

# Evaluation of the biodistribution and radiation dosimetry of the $^{18}$F-labelled amyloid imaging probe [$^{18}$F]FACT in humans

Miho Shidahara[1,2*], Manabu Tashiro[2], Nobuyuki Okamura[3], Shozo Furumoto[3], Katsutoshi Furukawa[4], Shoichi Watanuki[2], Kotaro Hiraoka[2], Masayasu Miyake[2], Ren Iwata[5], Hajime Tamura[1], Hiroyuki Arai[4], Yukitsuka Kudo[6] and Kazuhiko Yanai[2,3]

**Abstract**

**Background:** The biodistribution and radiation dosimetry of the $^{18}$F-labelled amyloid imaging probe ([$^{18}$F] FACT) was investigated in humans.

**Methods:** Six healthy subjects (three males and three females) were enrolled in this study. An average of 160.8 MBq of [$^{18}$F] FACT was intravenously administered, and then a series of whole-body PET scans were performed. Nineteen male and 20 female source organs, and the remainder of the body, were studied to estimate time-integrated activity coefficients. The mean absorbed dose in each target organ and the effective dose were estimated from the time-integrated activity coefficients in the source organs. Biodistribution data from [$^{18}$F] FACT in mice were also used to estimate absorbed doses and the effective dose in human subjects; this was compared with doses of [$^{18}$F] FACT estimated from human PET data.

**Results:** The highest mean absorbed doses estimated using human PET data were observed in the gallbladder (333 ± 251 μGy/MBq), liver (77.5 ± 14.5 μGy/MBq), small intestine (33.6 ± 30.7 μGy/MBq), upper large intestine (29.8 ± 15.0 μGy/MBq) and lower large intestine (25.2 ± 12.6 μGy/MBq). The average effective dose estimated from human PET data was 18.6 ± 3.74 μSv/MBq. The highest mean absorbed dose value estimated from the mouse data was observed in the small intestine (38.5 μGy/MBq), liver (25.5 μGy/MBq) and urinary bladder wall (43.1 μGy/MBq). The effective dose estimated from the mouse data was 14.8 μSv/MBq for [$^{18}$F] FACT.

**Conclusions:** The estimated effective dose from the human PET data indicated that the [$^{18}$F] FACT PET study was acceptable for clinical purposes.

**Keywords:** Positron emission tomography, Radiation dosimetry, Amyloid imaging, MIRD, [$^{18}$F] FACT

## Background

### Amyloid beta imaging

Deposits of amyloid β (Aβ) plaque are one of the pathological observations in patients with Alzheimer's disease (AD); Aβ deposition progresses at an earlier point than the current clinical diagnostic point for this disease [1]. For earlier diagnosis of AD and the evaluation of treatment efficacy, *in vivo* amyloid imaging using positron emission tomography (PET), which provides quantitation and visualisation of Aβ deposition in the brain, is useful. Therefore, several Aβ-binding probes dedicated for PET imaging have been developed [2,3].

Most of these PET Aβ ligands are $^{11}$C-labelled compounds (physical half life ($T_{1/2}$), 20 min), and $^{18}$F-labelled agents are being increasingly investigated owing to their long half life ($T_{1/2}$, 109.7 min). The long $T_{1/2}$ of $^{18}$F enables several PET scans to be carried out from a single synthesis of labelled agent and also enables its commercial distribution to any PET facility. On the other hand, the longer the $T_{1/2}$ of the radioisotope gets, the greater is the radiation

* Correspondence: shidahara@med.tohoku.ac.jp
[1]Division of Medical Physics, Tohoku University School of Medicine, 2-1 Seiryo-machi, Aoba-ku, Sendai 980-8575, Japan
[2]Division of Cyclotron Nuclear Medicine, Cyclotron Radioisotope Center, Tohoku University, Sendai 980-8578, Japan
Full list of author information is available at the end of the article

dose exposure for the PET subject for the same administered dose of radioligand.

### Importance of radiation dosimetry

For subjects undergoing PET, internal radiation exposure is inevitable, and the radiation dose delivered is proportional to the level of radioactivity of the injected radioligand and the number of injections. In the case of amyloid imaging, subjects often have multiple PET scans for diagnostic or therapeutic longitudinal monitoring of Aβ aggregation in the brain. Therefore, estimation of the radiation dose exposure from each PET radioligand and the use of well-balanced PET scan protocols taking into consideration subject risk and benefit are important.

Estimation of the internal radiation dose requires a time series measurement of the biodistribution of the injected radioligand. There are two ways to establish the biodistribution of a radioligand in humans: one is to extrapolate from data obtained in animal experiments [4] and the other is to use data from a clinical whole-body PET study [5]. Data extrapolated from animal experiments have been used to estimate clinical radiation dose. However, Sakata et al. reported that in some radioligands, there were considerable differences in organ dose or kinetics between human and animal experiments and that a whole-body PET study would be desirable for the initial clinical evaluation of new PET radioligands [6].

### Previous biodistribution and dosimetry study for PET amyloid imaging

Recently, radiation dose exposures from several PET amyloid imaging agents have been reported using clinical whole-body PET scans. One of the popular amyloid ligands, Pittsburgh compound B ([$^{11}$C]PIB), has been extensively investigated with regard to its kinetics in the human body, and its effective radiation dose was found to be 4.74 μSv/MBq on average [7]. For $^{18}$F-labelled PET amyloid radioligands, effective doses in humans have been reported as follows: $^{18}$F-AV-45, 13 and 19.3 μSv/MBq [8,9]; $^{18}$F-GE067, 33.8 μSv/MBq [10]; and $^{18}$F-BAY94-9172, 14.7 μSv/MBq [11].

### Aim of the present study

Fluorinated amyloid imaging compound ([$^{18}$F]FACT) is an $^{18}$F-labelled amyloid imaging agent developed at Tohoku University [12]. Kudo and colleagues at this university have previously developed a $^{11}$C amyloid imaging agent named [$^{11}$C]BF-227 [3]. [$^{18}$F]FACT is derived from [$^{11}$C]BF-227 by reducing its lipophilicity in order to reduce the nonspecific binding in the brain; AD patients showed significantly higher uptake of [$^{18}$F]FACT in the neocortex region relative to controls [12]. However, the biodistribution of [$^{18}$F]FACT in humans has not yet been investigated.

In the present study, the radiation dosimetry and biodistribution of [$^{18}$F]FACT was investigated in healthy elderly subjects who are the target group for PET amyloid imaging. In order to determine the discrepancy in the estimated radiation dose between human and animal experiments, biodistribution studies in mice involving [$^{18}$F]FACT were also conducted.

## Methods

### Subjects

PET studies were performed in three healthy male and in three healthy female volunteers (mean age ± standard deviation (SD), 76.3 ± 3.2 years). Subject characteristics are shown in Table 1. Both height and weight varied over a wide range (146 to 175 cm and 39 to 74 kg, respectively). All subjects were Japanese and were free of somatic and neuropsychiatric illness, as determined by clinical history and physical examination; one male subject (no. 1) had undergone a previous surgical operation involving gallbladder removal.

This study was approved by the Ethics Committee on Clinical Investigations of Tohoku University School of Medicine and was performed in accordance with the Declaration of Helsinki. Written informed consent was obtained from all subjects after a complete description of the study had been made.

### Radiochemistry and radioligand purity

Figure 1 shows the chemical structure of $^{18}$F-FACT. The radiochemical purity of the radioligand in the present clinical study ranged from 97.8% to 98.7% (mean ± SD, 98.33 ± 0.42%). The specific radioactivity ranged from 30.6 to 347.7 GBq/μmol at the time of injection (mean ± SD, 139.9 ± 116.2 GBq/μmol).

### PET study

All whole-body PET studies were performed using a SET-2400W scanner (Shimadzu Inc., Kyoto, Japan) in two-dimensional (2D) mode [13]. The PET scanner acquired 63 image slices at a centre-to-centre interval of 3.125 mm and had a spatial resolution of 3.9 mm full width at half maximum (FWHM) and a *Z*-axis resolution of 6.5 mm FWHM at centre field of view [13].

An overview of scan protocols is shown in Figure 2. Four emission scans and two transmission scans (before administration and intermediate emission scans) using a $^{68}$Ge/$^{68}$Ga source were performed, with the exception of subject no. 1 who had three emission scans. In the present series of PET studies and in other research projects, a 15-min PET brain scan using three-dimensional (3D) mode was performed after the first emission scan. At 2 min after intravenous administration of 142 to 180 MBq [$^{18}$F]FACT (mean ± SD, 160.8 ± 14.8 MBq; injection mass, 0.77 ± 0.66 ng), a series of whole-body PET

**Table 1 Information regarding the human subjects**

| | Sex | Age (years) | Height (m) | Weight (kg) | BMI (kg/m$^2$) | History |
|---|---|---|---|---|---|---|
| Subject number | | | | | | |
| 1 | M | 77 | 1.59 | 61.2 | 24.2 | Surgical removal of gallbladder |
| 2 | M | 78 | 1.62 | 65 | 24.8 | - |
| 3 | M | 77 | 1.75 | 74 | 24.2 | - |
| 4 | F | 70 | 1.46 | 39 | 18.3 | - |
| 5 | F | 77 | 1.56 | 60.2 | 26.1 | - |
| 6 | F | 79 | 1.55 | 56 | 23.3 | - |
| Mean ± 1 SD | | 76.3 ± 3.2 | 1.58 ± 0.75 | 59.2 ± 11.6 | 23.5 ± 2.7 | |

scans were performed. The schedule for the first and second transmission scans and the first, second, third and fourth emission scans was as follows: 6 positions × 4 min (24 min), 6 positions × 4 min (24 min), 6 positions × 3 min (18 min), 6 positions × 3 min (18 min), 6 positions × 3 min (18 min), and 6 positions × 4 min (24 min), respectively. The starting time of the second emission scan was different for each subject and was on average 55 min after the start of injection with a 5-min SD. The time gap between bed positions was 5 s. All emission data were reconstructed using OS-EM with iteration 16 and subset 2 after attenuation correction. Scatter correction was not performed because of the use of 2D mode data acquisition. The cross calibration factor of the scanner (Bq per ml/cps per voxel) was determined once per week using a cylindrical water phantom (25-cm length and 20-cm inner diameter) filled with $^{18}$F solutions and by measuring the sample activity of the $^{18}$F solutions at the well counter (BSS-3: Shimadzu Co., Ltd., Kyoto, Japan) [14].

Urination was controlled before, after and during the series of PET studies. In particular, during (15 min after the end of the first emission scan) and after the PET scans, subjects were asked to void. The volume and radioactivity levels of their urine samples were measured using a calibrated well counter.

### MRI study

All subjects underwent T1-weighted magnetic resonance imaging (MRI) scans using a Signa 1.5-T machine (General Electric Inc., Milwaukee, WI, USA) within a week of the PET scans. For each position (brain, chest, abdomen and epigastric region), individual T1-weighted scans with a voxel size of 1.875 × 1.875 × 6.000 mm (TR = 460 ms, TE = 14 ms, image matrix = 256 × 256 × 40) were obtained with subjects holding their breath.

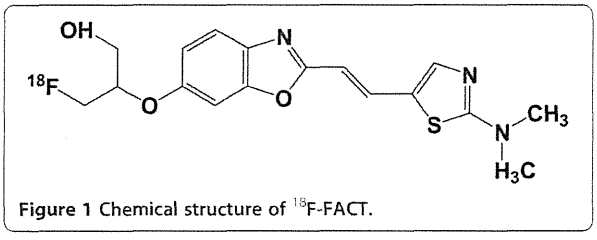


**Figure 1** Chemical structure of $^{18}$F-FACT.

### Dosimetry

The Medical Internal Radiation Dose committee of the Society of Nuclear Medicine developed the algorithm to calculate absorbed dose $D$ (the energy deposited per unit mass of medium (Gy)) in organs. The basic idea is that radiation energy from the radioisotope in the source organ is absorbed in the target organs, and the algorithm requires the net accumulated radioactivity in source organs as an input [15]. A PET scan contributes to quantitative knowledge on the whole-body distribution of radioisotope. In the present study, the accumulated activity in source organs was derived from PET measurements and the organ volumes of the reference male or female. The mean absorbed dose to the $k$th target organ is defined as follows:

$$\bar{D}(r_k) = \sum_h \tilde{A}_h \times S(r_k \leftarrow r_h) = \sum_h A_0 \times \tau_h \times S(r_k \leftarrow r_h),\ \tau_h = \frac{\tilde{A}_h}{A_0} \quad (1)$$

where $S(r_k \leftarrow r_h)$ is the absorbed dose in the $k$th target organ per unit of accumulated activity in the $h$th source organ, called the $S$ value. $\tilde{A}_h$ is the number of disintegrations in the $h$th source organ, $A_0$ is the injected dose, and $\tau_h$ is the time-integrated activity coefficient in the $h$th source organ (equal to the number of disintegrations per unit activity administered). The effective dose $E$ (Sv), as defined by the International Commission on Radiological Protection (ICRP) 60 [10], was obtained using the following equation:

$$E = \sum_i Q \times w_i \times D_i \quad (2)$$

where $D_i$ is the absorbed dose of the $i$th target organ, $w_i$ is the weighting risk factor in the $i$th target organ, and $Q$ is the quality factor ($Q$ = 1 for β- and γ-rays).

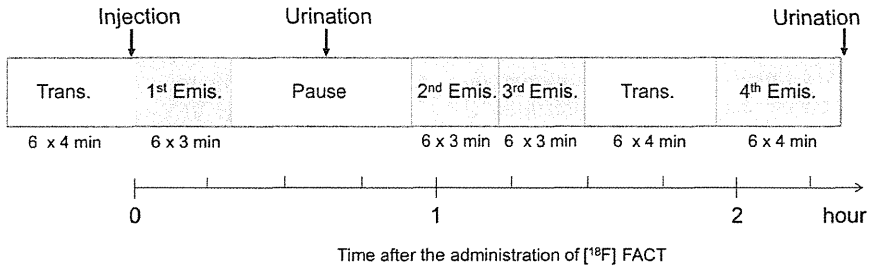


**Figure 2 Overview of PET scan protocols.** Four emission scans and two transmission scans (before and intermediate emission scans) with a $^{68}Ge/^{68}Ga$ source were performed. In particular, the second transmission scan was performed using a post-injection transmission scan.

### Regions of interest

The number of source organs used for region-of-interest (ROI) drawing was 19 for male and 20 for female subjects. A detailed list of source organs is shown in Table 2. Two nuclear medicine physicians manually drew the ROIs using PMOD version 3.1 (PMOD Technologies, Zurich, Switzerland). All individual PET images and MRI images were co-registered to the first individual PET images using a rigid matching module of the same PMOD with a dissimilarity function of normalised mutual information (for MRI-to-PET cases) and the sum of the absolute difference (for PET-to-PET cases) algorithms.

For visceral organs with extremely high uptake (liver and gallbladder), individual ROIs were defined at a fixed

**Table 2 [$^{18}$F]FACT time-integrated activity coefficients in the source organs**

| Organ | Human (MBq-h/MBq) | | | | | | | Mouse (MBq-h/MBq) |
|---|---|---|---|---|---|---|---|---|
| | Mean ± 1 SD | Subject 1 | Subject 2 | Subject 3 | Subject 4 | Subject 5 | Subject 6 | |
| Adrenal gland | 5.38E−04 ± 2.98E−04 | 9.40E−04 | 8.40E−04 | 5.20E−04 | 3.70E−04 | 4.00E−04 | 1.60E−04 | - |
| Brain | 4.20E−02 ± 8.44E−03 | 5.41E−02 | 3.68E−02 | 3.53E−02 | 4.87E−02 | 4.42E−02 | 3.26E−02 | 6.99E−03 |
| Breast | 8.40E−03 ± 4.37E−03 | 1.14E−03 | 8.25E−03 | 5.59E−03 | 1.16E−02 | 1.19E−02 | 1.19E−02 | - |
| Gallbladder content[a] | 2.22E−01 ± 1.05E−01 | - | 1.49E−01 | 2.27E−01 | 3.88E−01 | 1.16E−01 | 2.31E−01 | - |
| Lower large intestine content | 2.12E−02 ± 2.03E−02 | 5.91E−02 | 1.06E−02 | 4.80E−03 | 2.27E−02 | 2.40E−02 | 5.96E−03 | - |
| Small intestine content | 8.78E−02 ± 1.08E−01 | 7.40E−02 | 3.74E−02 | 3.34E−02 | 3.06E−01 | 3.36E−02 | 4.25E−02 | 1.22E−01 |
| Stomach content | 6.71E−03 ± 2.28E−03 | 5.22E−03 | 6.23E−03 | 9.29E−03 | 9.84E−03 | 4.78E−03 | 4.87E−03 | - |
| Upper large intestine content | 2.55E−02 ± 1.89E−02 | 1.48E−02 | 4.88E−02 | 1.01E−02 | 4.99E−02 | 2.04E−02 | 8.85E−03 | - |
| Heart content | 1.12.E−02 ± 1.51E−03 | 1.24E−02 | 1.13E−02 | 1.02E−02 | 1.30E−02 | 1.15E−02 | 8.83E−03 | 3.95E−03 |
| Heart wall | 7.50E−03 ± 1.84E−03 | 4.63E−03 | 1.00E−02 | 8.84E−03 | 6.75E−03 | 7.28E−03 | 7.49E−03 | 2.39E−03 |
| Kidney | 1.34E−02 ± 3.27E−03 | 1.32E−02 | 1.16E−02 | 1.53E−02 | 1.89E−02 | 9.59E−03 | 1.20E−02 | 9.34E−03 |
| Liver | 4.92E−01 ± 1.05E−01 | 6.28E−01 | 5.85E−01 | 4.34E−01 | 5.15E−01 | 3.42E−01 | 4.49E−01 | 1.69E−01 |
| Lung | 3.55E−02 ± 1.16E−02 | 3.78E−02 | 5.31E−02 | 4.36E−02 | 2.46E−02 | 2.33E−02 | 3.08E−02 | 1.17E−02 |
| Muscle | 4.66E−01 ± 3.73E−01 | 9.43E−01 | 5.47E−01 | 7.97E−01 | 5.40E−02 | 4.12E−01 | 4.34E−02 | 1.57E−01 |
| Ovary[b] | 5.53E−04 ± 3.79E−05 | - | - | - | 5.70E−04 | 5.10E−04 | 5.80E−04 | - |
| Pancreas | 4.13E−03 ± 9.75E−04 | 6.10E−03 | 3.62E−03 | 3.93E−03 | 3.81E−03 | 3.55E−03 | 3.76E−03 | - |
| Red marrow | 3.98E−02 ± 4.33E−03 | 4.02E−02 | 3.83E−02 | 3.79E−02 | 4.59E−02 | 4.29E−02 | 3.34E−02 | 1.61E−02 |
| Spleen | 5.41E−03 ± 1.74E−03 | 8.64E−03 | 4.88E−03 | 3.83E−03 | 6.01E−03 | 4.77E−03 | 4.30E−03 | 1.28E−03 |
| Testis[c] | 5.77E−04 ± 4.67E−04 | 7.00E−04 | 6.10E−05 | 9.70E−04 | - | - | - | - |
| Thyroid | 3.53E−04 ± 1.55E−04 | 6.30E−04 | 3.70E−04 | 3.60E−04 | 2.40E−04 | 1.80E−04 | 3.40E−04 | - |
| Urinary bladder contents | 2.26E−02 ± 8.36E−03 | 1.70E−02 | 2.69E−02 | 1.55E−02 | 3.63E−02 | 2.49E−02 | 1.51E−02 | 6.56E−02 |
| Uterus/uterine wall[b] | 4.46E−03 ± 1.90E−03 | - | - | - | 6.42E−03 | 2.63E−03 | 4.33E−03 | - |
| Remainder of the body | 1.17 ± 3.63E−01 | 7.24E−01 | 1.06 | 9.48E−01 | 1.08 | 1.51 | 1.69 | 2.08 |

Averaged time-integrated activity coefficient (MBq-h/MBq) for the source organs ($n$ = 6) from the whole-body PET data ($n$ = 6) from experiments involving human subjects of [$^{18}$F]FACT and mice of [$^{18}$F]FACT. [a]Averaged value among five subjects excluding subject no. 1. [b]Average time-integrated activity coefficient among female subjects ($n$ = 3). [c]Average time-integrated activity coefficient among male subjects ($n$ = 3).

emission scan with about a 40% threshold against the maximum counts (first emission for the liver and third or fourth emission for the gallbladder). Then the ROI was applied to the other emission images with minor adjustment of its location or shape. For the intestines, if specific high uptake was observed, individual ROIs were defined on each time frame of the PET images with about a 10% threshold. If there was no specific high uptake in the intestines, and uptake could be regarded as uniform, individual ROIs were drawn around the corresponding area.

In order to obtain a typical radioactivity concentration within organs with less location mismatch between PET and the co-registered MRI images (brain, breast, heart wall, heart contents, kidney, liver, lung, muscle, bones, spleen and thyroid), individual ROIs were drawn on co-registered MRI images. For other low-uptake organs (adrenal gland, stomach contents, pancreas, ovary, uterus and testis), individual ROIs were drawn on each time frame of the PET images and referred to the co-registered MRI images. To avoid a partial volume effect, the size of the ROI for these MRI available organs was made slightly smaller than the entire source organ. It should also be noted that all activities in vertebrae ROIs was assumed to be in the red marrow in the present study.

### Data analysis

Averaged time-activity curves for each organ were obtained using the ROI values from each subject's PET images. Because the PET images were decay-corrected at the start of each scan during the reconstruction procedure, the non-decay-corrected time-activity curves ($C$(t), Bq/ml) were re-calculated. During each whole-body emission scan, the bed position was moved from the foot to the head (six bed positions in total). However, we assumed that PET counts at all bed positions were acquired at the mid-scan time. Then, individual radioactivity concentration per injected dose $A_0$ (Bq) was extrapolated into the percent injected dose (%ID) of the reference subject as follows:

$$\%\mathrm{ID}(t)_{\mathrm{reference}} = \left(\frac{C(t)}{A_0}\right)_{\mathrm{individual}} \times V_{\mathrm{reference}} \qquad (3)$$

where $V$ (ml) is the organ volume, and $V_{\mathrm{reference}}$ is $V$ of the reference subject (we used a 70-kg adult male and 58-kg adult female as the male and female reference subjects) [16,17]. Even though some organs such as the intestine may change their volume over time, we used the reference subjects' organ volumes over the time period of the calculation of the %ID.

The time-integrated activity coefficient $\tau$ (Bq-h/Bq) in Equation 1 was obtained by fitting (%ID($t$)) using a mono-exponential function and integrating from time zero to infinity. If the time-activity curve did not converge at the last PET scan (e.g. intestines and gallbladder), time-activity curves were fitted using two exponential functions, and then the area under the curve after the acquisition of the last image was calculated by assuming only physical decay of $^{18}$F and no additional biologic clearance to be conservative [10]. The time-integrated activity coefficient for urinary bladder content was calculated by applying the dynamic urinary bladder model [10] to the urine samples with a bladder voiding interval of 2 h. The decay-corrected cumulative activity for urine was fitted using the equation $A \times (1 - \exp(-\ln(2) \times t / \tau))$, where $\tau$ is the biological decay and $A$ is the fraction of activity released from the body. The sum of the time-integrated activity coefficient for the specific organs was subtracted from the time-integrated activity coefficient for the total body, which was calculated from the time integral of the decaying injected radioactivity. Then the residual of the subtraction was regarded as the time-integrated activity coefficient in the remainder of the body. All fitting procedures were undertaken using a mean fit of $R^2$ of 0.93 ± 0.13.

Finally, the time-integrated activity coefficient $\tau$ (Bq-h/Bq) was used to calculate the absorbed dose, $D$, in Equation 1 and the effective dose, $E$, in Equation 2. Both kinetics calculations (fitting and integration) and dose estimation were performed using OLINDA/EXM software version 1.0 (Department of Radiology and Radiological Sciences Vanderbilt University, Nashville, TN, USA) [17].

### Animal experiments

The experimental protocols were reviewed by the Committee on the Ethics of Animal Experiments at Tohoku University School of Medicine and performed in accordance with the Guidelines for Animal Experiments issued by the Tohoku University School of Medicine. Estimated radiation dose of [$^{18}$F]FACT in the human subjects calculated from mouse data sets was compared with those of [$^{18}$F]FACT from human whole-body PET scans. An average dose of 1.4 MBq of [$^{18}$F]FACT was intravenously injected into ICR mice (age, 6 weeks; average body weight, 30 g) without anaesthesia. In the [$^{18}$F]FACT study, the mice were killed by cervical luxation at 2, 10, 30, 60 and 120 min ([$^{18}$F]FACT) after administration ($n$ = 4 at each time point). The masses of the blood, heart, lung, liver, spleen, small intestine, kidney, brain and urine samples were measured, and activity was also measured using a well counter. Thigh bone and muscle were also sampled. The average uptake of the

radioligand into the male reference subject (70 kg) was extrapolated as follows [18]:

$$\%\mathrm{ID}(t)_{\mathrm{human}} = \left(\frac{\%\mathrm{ID}(t)}{\mathrm{mass}_{\mathrm{organ}}}\right)_{\mathrm{mouse}} \times \left(\mathrm{mass}_{\mathrm{body}}\right)_{\mathrm{mouse}} \times \left(\frac{\mathrm{mass}_{\mathrm{organ}}}{\mathrm{mass}_{\mathrm{body}}}\right)_{\mathrm{human}} \quad (4)$$

where the bodyweight of the mouse was assumed to be 30 for [$^{18}$F]FACT.

Finally, in the same manner as in the human PET data analysis, time-integrated activity coefficients, absorbed doses and effective doses were calculated using the OLINDA/EXM software version 1.0. Sampled blood, thighbone and urine were regarded as heart contents, red bone marrow and urinary bladder contents, respectively.

## Results and discussion

### Biodistribution of [$^{18}$F]FACT

Figure 3A is the coronal PET image for a single female subject (no. 5) and demonstrates the typical biodistribution of [$^{18}$F]FACT in the human body. The highest accumulations of this radioligand were observed in the gallbladder, liver, intestine and urinary bladder. For subject no. 1, [$^{18}$F]FACT contained in the bile was excreted from the liver to the duodenum through the biliary tract (Figure 3B). The biodistribution pattern of [$^{18}$F]FACT in human subjects showed a predominant hepatobiliary excretion, which is similar to what has been observed for other amyloid ligands, such as [$^{11}$C]PIB, [$^{18}$F]AV-45, [$^{18}$F]GE067 and [$^{18}$F]BAY94-9172 [7,8,10,11].

Figure 4 shows the decay-corrected time-activity curve of the %ID for typical source organs (brain, liver, spleen, lung, kidney, heart content, heart wall, muscle, red marrow, small intestine contents, gallbladder, upper large intestine contents and urinary bladder) from the six volunteers and the mice experiments. A significant difference between the %ID from humans and mice was observed in the brain, liver, spleen, heart contents, red marrow and urinary bladder, and these differences propagated the different results regarding dose estimation. In human subjects, $^{18}$F uptake in the gallbladder contents and the intestines (Figure 4J,K,L) indicated larger individual variations in radioactivity uptake relative to other organs (e.g. the kidney as shown in Figure 4E). Radioactivity uptake in the upper large intestine showed propagation of both ligand kinetics and inter-subject variation from the gallbladder (Figure 4K,L). Scheinin et al. previously reported that inter-subject variation in ligand uptake ([$^{11}$C]PIB) in the gallbladder may be due to the quality and quantity of post-injection food intake [7]. In the present study, the subjects drank water during the interval between the first and second PET scans. This may have been responsible for the increase in inter-subject variation regarding the gallbladder. Furthermore, because the gallbladder uptake in some subjects had declined or remained at a low level at the final time points, we assumed that there was only physical radioactive decay after the last PET scans. However, this assumption may have led to a conservative estimation of the absorbed dose.

Figure 5 presents typical brain PET images obtained using [$^{18}$F]FACT at different time points with an

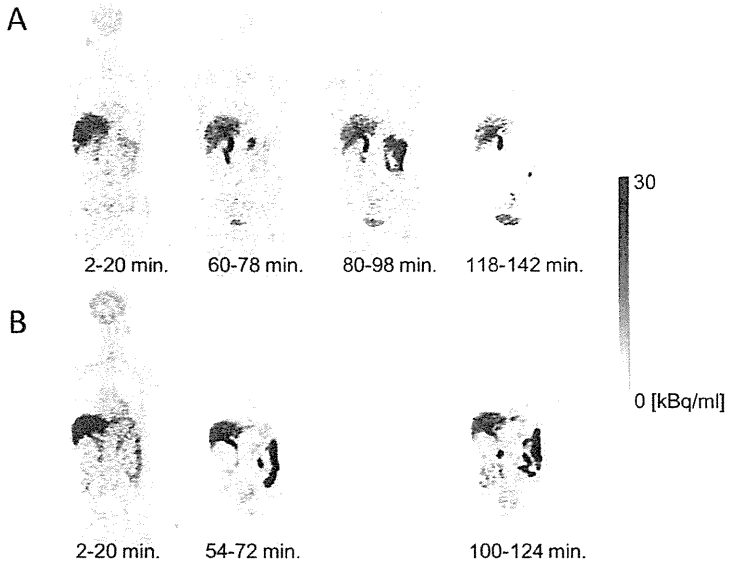


**Figure 3 Decay-corrected coronal radioactivity distributions.** Subject no. 5 (**A**) and subject no. 1 (**B**) at each PET measurement.

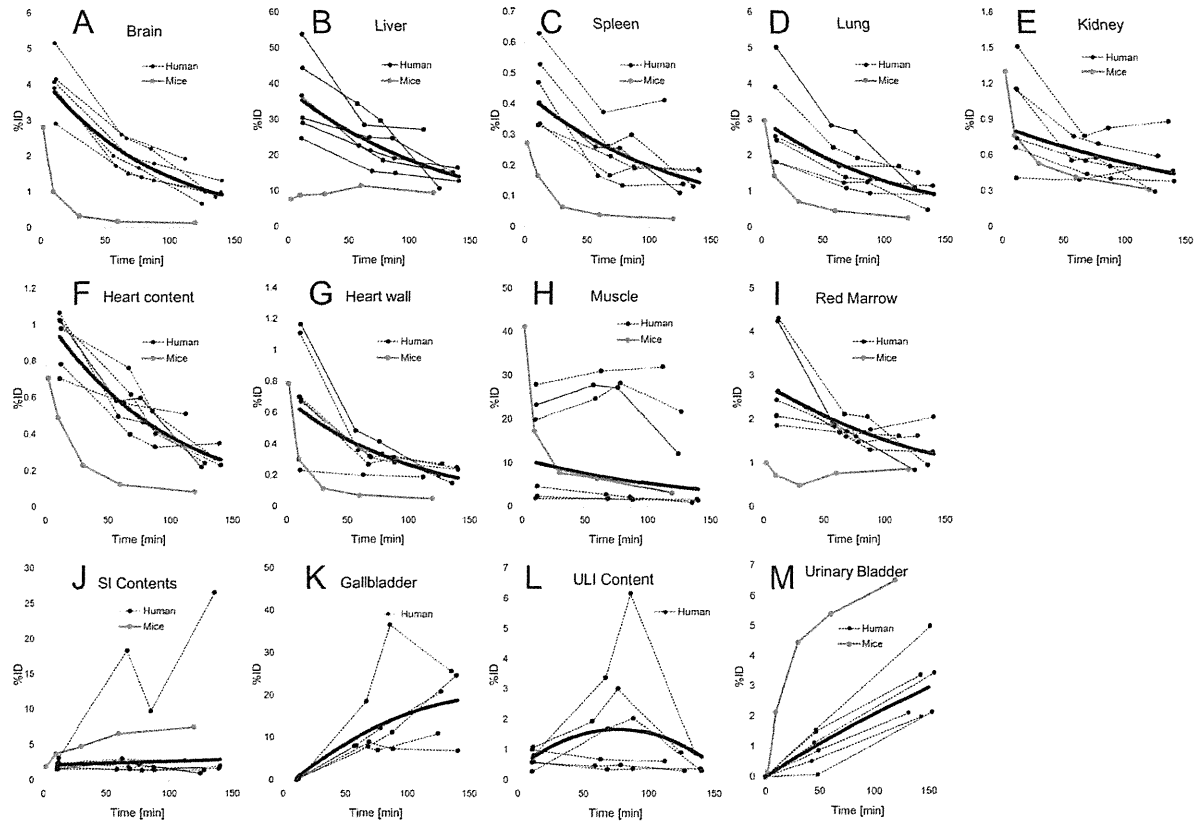


**Figure 4 Decay-corrected time-activity curves of %ID.** (**A**) Brain, (**B**) liver, (**C**) spleen, (**D**) lung, (**E**) kidney, (**F**) heart content, (**G**) heart wall, (**H**) muscle, (**I**) red marrow, (**J**) SI contents, (**K**) gallbladder, (**L**) ULI content and (**M**) urinary bladder for individual human (dashed black line) and averaged mice extrapolation ($n$ = 4 at each time point, grey line). The solid black line indicates fitted curve using exponential function from all subjects' data points. The urinary bladder curve indicates accumulated activity excreted at all voiding/sampling moments.

acquisition time of 3 min (first, second and third emission) and 4 min (fourth emission). There was no significant retention of [$^{18}$F]FACT in the brain, and this may have been because the subject was normal.

### Estimated dose of [$^{18}$F]FACT

The [$^{18}$F]FACT time-integrated activity coefficients in the source organs are shown in Table 2, and the absorbed doses are shown in Table 3. The averaged time-integrated activity coefficient for the gallbladder, as shown in Table 2, was calculated among five subjects excluding subject no. 1; however, in the case of the averaged absorbed and effective doses, subject no. 1 was included (Table 3).

High absorbed dose in humans was observed in the gallbladder (333 ± 251 μGy/MBq), liver (77.5 ± 14.5 μGy/MBq), small intestine (33.6 ± 30.7 μGy/MBq), upper large intestine (29.8 ± 15.0 μGy/MBq) and lower large intestine (25.2 ± 12.6 μGy/MBq). In mice, high absorbed doses were observed in the small intestine (38.5 μGy/MBq), liver (25.5 μGy/MBq) and urinary bladder wall (43.1 μGy/MBq) for [$^{18}$F]FACT (Table 3).

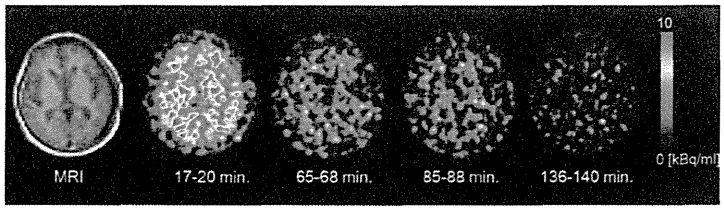


**Figure 5 Decay-corrected brain PET images of subject no. 3 at different time points.**

**Table 3 Absorbed doses in the source organs**

| | Human | | | Mouse |
|---|---|---|---|---|
| | All subjects ($n$ = 6) | Male ($n$ = 3) | Female ($n$ = 3) | |
| Organ | | | | |
| Adrenal gland | 1.96E01 ± 2.00 | 2.03E01 | 1.90E01 | 1.35E01 |
| Brain | 9.91 ± 1.82 | 8.95 | 1.09E01 | 4.17 |
| Breasts | 8.69 ± 2.55 | 6.68 | 1.07E01 | 9.90 |
| Gallbladder wall | 3.33E02 ± 2.51E02 | 2.16E02 | 4.50E02 | 1.68E01 |
| Lower large intestine wall | 2.52E01 ± 1.26E01 | 2.41E01 | 2.63E01 | 1.57E01 |
| Small intestine | 3.36E01 ± 3.07E01 | 2.07E01 | 4.64.E01 | 3.85E01 |
| Stomach wall | 1.61E01 ± 3.44 | 1.35E01 | 1.87E01 | 1.39E01 |
| Upper large intestine wall | 2.98E01 ± 1.50E01 | 2.36E01 | 3.59E01 | 1.83E01 |
| Heart wall | 1.62E01 ± 1.70 | 1.50E01 | 1.74E01 | 8.34 |
| Kidneys | 2.01E01 ± 4.30 | 1.85E01 | 2.17E01 | 1.32E01 |
| Liver | 7.75E01 ± 1.45E01 | 7.38E01 | 8.11E01 | 2.55E01 |
| Lungs | 1.46E01 ± 1.10 | 1.49E01 | 1.43E01 | 7.96 |
| Muscle | 1.03E01 ± 1.27 | 1.07E01 | 9.90 | 7.89 |
| Ovary | 1.67E01 ± 6.65 | 1.18E01 | 2.16E01 | 1.67E01 |
| Pancreas | 2.32E01 ± 3.11 | 2.17E01 | 2.47E01 | 1.45E01 |
| Red marrow | 1.31E01 ± 1.70 | 1.16E01 | 1.46E01 | 1.23E01 |
| Osteogenic cells | 1.60E01 ± 3.65 | 1.25E01 | 1.95E01 | 1.82E01 |
| Skin | 7.30 ± 1.39 | 5.99 | 8.60 | 8.70 |
| Spleen | 1.37E01 ± 2.48 | 1.27E01 | 1.48E01 | 7.83 |
| Testis | 7.32 ± 2.16 | 7.32 | - | 1.15E01 |
| Thymus | 1.00E01 ± 1.85 | 8.37 | 1.16E01 | 1.08E01 |
| Thyroid | 8.36 ± 1.38 | 8.86 | 7.86 | 1.10E01 |
| Urinary bladder wall | 2.23E01 ± 7.33 | 1.81E01 | 2.66E01 | 4.31E01 |
| Uterus | 1.67E01 ± 8.13 | 1.14E01 | 2.19E01 | 1.77E01 |
| Total body | 1.38E01 ± 1.63 | 1.22E01 | 1.53E01 | 1.22E01 |
| Effective dose (μSv/MBq) | 1.86E01 ± 3.74 | 1.64E01 | 2.09E01 | 1.48E01 |

Averaged absorbed dose estimates (μGy/MBq) for the target organs from the whole-body PET data ($n$ = 6) from experiments involving human subjects of [$^{18}$F]FACT and mice of [$^{18}$F]FACT. Average absorbed dose for male subjects ($n$ = 3).

The effective dose estimated from the human PET study was 18.6 ± 3.74 μSv/MBq. The effective doses of [$^{18}$F]FACT estimated from the clinical PET studies among other $^{18}$F-labelled PET amyloid radioligands were as follows: [$^{18}$F]AV-45, 13 and 19.3 μSv/MBq [8,9]; [$^{18}$F]GE067, 33.8 μSv/MBq [10]; and [$^{18}$F]BAY94-9172, 14.67 μSv/MBq [11]. For PET analysis of [$^{11}$C]PIB, Scheinin et al. normalised the %ID using the ratio of individual and reference subjects' body weights (Equation 4) [7]. However, in the present study, we did not normalise the %ID data because there was a small difference between the effective dose with normalisation (17.6 ± 2.12 μSv/MBq) and the present effective dose (18.6 ± 3.74 μSv/MBq). Therefore, we concluded that body weight normalisation does not influence the effective dose.

The effective dose of [$^{18}$F]FACT from the mouse experiments (14.8 μSv/MBq) was underestimated as compared with that from the human subject PET studies (18.6 μSv/MBq) (Table 3). This discrepancy corresponded to 0.76 mSv (2.96 and 3.72 mSv from mice and humans, respectively) while assuming an injected activity of 200 MBq as a clinically relevant dose. The underestimation of absorbed dose in the mouse gallbladder (20 times lower) and liver (3 times lower) relative to the human PET studies may have been responsible for the underestimation of the effective dose. High absorbed doses in the liver, gallbladder and small intestine of mice indicated that the biodistribution pattern of [$^{18}$F]FACT in mice includes hepatobiliary excretion, as was observed in the PET scans involving human subjects. However,

the estimated absorbed dose in the gallbladder was 20 times lower than the estimate from human subject data sets because we could not remove the gallbladder of the mouse. Therefore, to evaluate the effective dose of [$^{18}$F]FACT in target organs, a whole-body PET scan of human subjects may be preferable as compared with the extrapolation from mouse experiments.

### Clinical applicability of [$^{18}$F]FACT

The present whole-body PET study was performed using healthy elderly subjects and not patients with AD. Previously, Koole et al. speculated that if brain uptake of $^{18}$F amyloid ligand increased by a factor of three, this will only influence estimation of the effective dose within 1%; however, when the subject had taken medication that changed the function of the hepatic metabolism, the estimated effective dose will vary with a larger range [10].

In the present series of PET studies, brain PET scans using the 3D mode were performed between the first and the second emission scan. Therefore, the injected dose for 2D whole-body scans was set to lower level than usual, and the averaged injected activity of 160.8 MBq corresponded to a radiation dose of 2.99 mSv per single administration. With regard to the optimal injected activity that can ensure sufficient image quality for clinical use, the peak noise-equivalent counts ratio (NECR) is often used in its determination. It has also been reported that the peak NECR in 2D mode was not reached with an acceptable range of injected activity, whereas in 3D mode, there was a distinct maximum for the NECR for which the corresponding injected activity was based on patient height and weight [19]. For the scanner used in our study, the NECR peak in 3D mode was reached at 4.44 kBq/ml using an 8,000-ml phantom [13]. When the subject's height and weight were assumed to be 170 cm and 60 kg, respectively, this assumption corresponded to the optimal injected dose of about 260 MBq. In a real situation, there exists the effect of the activity outside the axial FOV, and the optimal injected dose would be much lower. Injected activity indicates radiation dose; for example, 200 MBq indicates a radiation dose of 3.72 mSv. ICRP 62 [20] recommended that the maximum radiation dose that causes a 'minor to intermediate' increase of risk levels while preserving social benefit levels that are 'intermediate to moderate' has an effective limit of 10 mSv/year [20,21]. Thus, the maximum injectable activity is 537.6 MBq [$^{18}$F]FACT/year, and this injection dose limit allows two or three PET scans to be performed. Furthermore, amyloid imaging is mainly undertaken in elderly patients aged >50 years, even though for early detection of AD, patients aged <50 years will also have an amyloid PET scan. According to the guidance on medical exposures in medical and biomedical research by the European Commission [22], dose restrictions for patients aged over >50 years are not as strict as for younger patients. Therefore, considerably more multiple PET scans may be possible.

## Conclusions

The effective dose of the $^{18}$F-labelled amyloid imaging agent, [$^{18}$F]FACT, was found to be acceptable for clinical study.

#### Competing interests

The authors declare that they have no competing interests.

#### Authors' contributions

MS carried out the data analysis and interpretation and drafted the manuscript. TM, HT, YK and KY performed the study design and contributed to the intellectual discussion. NO, SF and RI performed the animal experiments and synthesis of PET probes. KF, SW, KH, MM and HA provided the clinical data. All authors read and approved the final manuscript.

#### Acknowledgements

We would like to thank Dr. Muneyuki Sakata from the Positron Medical Center, Tokyo Metropolitan Institute of Gerontology, and Dr. Hiroshi Watabe from the Cyclotron Radioisotope Center, Tohoku University, for their helpful advice regarding data analysis. This study was supported in part by Grants-in-Aid of Young Scientists (B) (no. 24700445) from the Ministry of Education, Culture, Sports, Science and Technology (MEXT), Japanese Government.

#### Author details

[1]Division of Medical Physics, Tohoku University School of Medicine, 2-1 Seiryo-machi, Aoba-ku, Sendai 980-8575, Japan. [2]Division of Cyclotron Nuclear Medicine, Cyclotron Radioisotope Center, Tohoku University, Sendai 980-8578, Japan. [3]Department of Pharmacology, Tohoku University School of Medicine, Sendai 980-8575, Japan. [4]Department of Geriatrics and Gerontology, Division of Brain Sciences, Institute of Development, Aging and Cancer, Tohoku University, Sendai 980-8575, Japan. [5]Division of Radiopharmaceutical Chemistry, Cyclotron Radioisotope Center, Tohoku University, Sendai 980-8578, Japan. [6]Clinical Research, Innovation and Education Center, Tohoku University Hospital, Sendai 980-8574, Japan.

Received: 23 January 2013 Accepted: 8 April 2013
Published: 24 April 2013

#### References

1. Hardy J, Selkoe DJ: **The amyloid hypothesis of Alzheimer's disease: progress and problems on the road to therapeutics.** *Science* 2002, 297:353–356.
2. Furumoto S, Okamura N, Iwata R, Yanai K, Arai H, Kudo Y: **Recent advances in the development of amyloid imaging agents.** *Curr Top Med Chem* 2007, 7:1773–1789.
3. Kudo Y, Okamura N, Furumoto S, Tashiro M, Furukawa K, Maruyama M, Itoh M, Iwata R, Yanai K, Arai H: **2-(2-[2-Dimethylaminothiazol-5-yl]ethenyl)-6-(2-[fluoro]ethoxy)benzoxazole: a novel PET agent for in vivo detection of dense amyloid plaques in Alzheimer's disease patients.** *J Nucl Med* 2007, 48:553–561.
4. Sakata M, Wu J, Toyohara J, Oda K, Ishikawa M, Ishii K, Hashimoto K, Ishiwata K: **Biodistribution and radiation dosimetry of the alpha7 nicotinic acetylcholine receptor ligand [$^{11}$C]CHIBA-1001 in humans.** *Nucl Med Biol* 2011, 38:443–448.
5. Deloar HM, Fujiwara T, Shidahara M, Nakamura T, Watabe H, Narita Y, Itoh M, Miyake M, Watanuki S: **Estimation of absorbed dose for 2-[F-18]fluoro-2-deoxy-D-glucose using whole-body positron emission tomography and magnetic resonance imaging.** *Eur J Nucl Med Mol Imaging* 1998, 25:565–574.
6. Sakata M, Oda K, Toyohara J, Ishii K, Nariai T, Ishiwata K: **Direct comparison of radiation dosimetry of six PET tracers using human whole-body imaging and murine biodistribution studies.** *Ann Nucl Med* 2013, 27:285–296.
7. Scheinin NM, Tolvanen TK, Wilson IA, Arponen EM, Nagren KA, Rinne JO: **Biodistribution and radiation dosimetry of the amyloid imaging agent $^{11}$C-PIB in humans.** *J Nucl Med* 2007, 48:128–133.